



Composite Structured Surfaces for Durable Dropwise Condensation

Ho Chan Chang^a, Manjunath C. Rajagopal^a, Muhammad Jahidul Hoque^a, Junho Oh^a, Longnan Li^a, Jiaqi Li^a, Hanyang Zhao^a, Gowtham Kuntumalla^a, Sreenath Sundar^a, Yuquan Meng^a, Chenhui Shao^a, Placid M. Ferreira^a, Srinivasa M. Salapaka^a, Sanjiv Sinha^a, Nenad Miljkovic^{a,b,c,d,*}



^a Department of Mechanical Science and Engineering, University of Illinois at Urbana-Champaign, Urbana, Illinois, 61801, USA

^b Department of Electrical and Computer Engineering, University of Illinois at Urbana-Champaign, Urbana, Illinois, 61801, USA

^c Materials Research Laboratory, University of Illinois at Urbana-Champaign, Urbana, Illinois, 61801, USA

^d International Institute for Carbon Neutral Energy Research (WPI-I2CNER), Kyushu University, 744 Moto-oka, Nishi-ku, Fukuoka, 819-0395, Japan

ARTICLE INFO

Article history:

Received 19 November 2019

Revised 19 April 2020

Accepted 27 April 2020

Available online 22 May 2020

Keywords:

Dropwise
Condensation
Composite
Coating
Hydrophobic
Structure
Micro
Nano
Metal
Polymer

ABSTRACT

Dropwise condensation of steam on hydrophobic substrates has a 10X higher heat transfer coefficient compared to filmwise condensation. To promote dropwise condensation, low surface energy hydrophobic coatings (polymers) are typically utilized. The low intrinsic thermal conductivity ($k < 1 \text{ W}/(\text{m}\cdot\text{K})$) of polymers, coupled with high heat transfer coefficient of dropwise condensation (100 $\text{kW}/(\text{m}^2\cdot\text{K})$), necessitates that the coating be thin ($< 1\mu\text{m}$) in order to avoid reducing the overall heat exchanger conductance. However, thin polymeric films easily degrade. The two opposing requirements result in the need for optimization between the durability (thick coating) and the heat transfer (thin coating). To enable high thermal conductivity in thicker coatings, we develop metal-polymer structured surfaces. By using porous structures as inter-connected heat-conducting backbones that are filled with hydrophobic materials, we enable tuning of the coating effective thermal conductivity and surface energy. Three metal structures were studied: micro/nanowires, inverse opals, and sintered spheres. Heat transfer performance was calculated using three-dimensional finite element method simulations with two distinct boundary conditions: convection at the walls and isothermal walls. Interestingly, the overall conductance shows up to 40% difference depending on the boundary condition used in calculating the composite coating effective thermal conductivity. We use our model to predict the heat transfer performance as a function of metal fraction by volume and by surface area for condensation. By coupling our thermal simulations with a previously verified analytical model for predicting wetting behavior on heterogeneous surfaces, we propose a regime map to predict dropwise-to-filmwise transition. Our work not only forms a starting point for the development of durable dropwise condensing surfaces, it identifies important considerations needed for computing effective thermal conductivity of composites.

© 2020 Elsevier Ltd. All rights reserved.

1. Introduction

Condensation heat transfer is a vital process for a plethora of industrial applications including power generation [1–6], thermal management [7–9], air conditioning [10], thermal-based water desalination, atmospheric water harvesting or dehumidification [11–14], and self-cleaning [15,16]. Enhancements to condensation heat transfer can potentially increase the overall efficiency of these systems [10]. When steam condenses on a low surface energy, hydrophobic substrate (e.g. a polymer), it condenses in a dropwise

fashion which is distinct from the thin liquid film that forms when condensing on a high surface energy, hydrophilic surface (e.g. a clean metal oxide). Dropwise condensation, typified by the formation of discrete water droplets which coalesce, shed, and clear the surface for re-nucleation, has the potential to achieve a 10X higher heat transfer coefficient when compared to filmwise condensation [5,17]. Appropriate hydrophobic promoters or coatings can lower the surface energy [3,5] and enable dropwise condensation on the metallic surfaces of common heat exchangers.

More than eight decades of research has conclusively demonstrated a lack of long-term durability (> 5 years) of hydrophobic coatings during dropwise condensation of steam, making industrial implementation difficult [5,18–20]. The fundamental bottleneck is the coating conundrum: sufficiently thick hydrophobic coatings

* Corresponding Author: 105 S. Mathews Avenue, Mechanical Engineering Laboratory, Room 2136, Urbana, IL 61801, USA.

E-mail address: nmiljkov@illinois.edu (N. Miljkovic).

Nomenclature

A	Total surface area (m^2)
D	Diameters of wires/pores/spheres (m)
d	Distance between two adjacent elements (inverse opals and sintered spheres) (m)
d_n	Neck diameter (inverse opals and sintered spheres) (m)
h	Heat transfer coefficient ($\text{W}/(\text{m}^2 \cdot \text{K})$)
k	Thermal conductivity ($\text{W}/(\text{m} \cdot \text{K})$)
k_p	Polymer thermal conductivity, $k_p = 0.1 \text{ W}/(\text{m} \cdot \text{K})$ throughout the analysis
L	Side length of a unit cell (m)
q	Heat transfer rate (W)
R	Thermal resistance (K/W)
T	Temperature ($^\circ\text{C}$)
t	Thickness of the coating (m)
U	Overall heat transfer coefficient ($\text{W}/(\text{m}^2 \cdot \text{K})$)
θ	Contact angle ($^\circ$)
ϕ	Metal surface fraction at the coating-vapor interface
ψ	Metal volume fractions of coating
f	Area fraction
Δ	Change
$\Delta\theta$	Contact angle hysteresis ($^\circ$)

Subscripts

A,m	Advancing state, metal surface
A,p	Advancing state, polymer surface
R,m	Receding state, metal surface
R,p	Receding state, polymer surface
Bruggeman	Bruggeman model for effective thermal conductivity
coating	Property of the coating
eff	Effective property of the composite
$i, 2$	Top and bottom surfaces that are isothermal
i	Internal side, or tube side
e	External side, or shell side
h	Convection boundary condition
T	Isothermal boundary condition
sub	Substrate
m	Metal
Maxwell	Maxwell model for effective thermal conductivity
n	Neck
p	Polymer
A	Advancing state
R	Receding state

$(> 10 \mu\text{m})$ are required to achieve durable dropwise condensation, while thin coatings ($< 1 \mu\text{m}$) are required for low parasitic thermal resistance due to the low intrinsic thermal conductivity of polymers ($k \sim 0.1 \text{ W}/(\text{m} \cdot \text{K})$) [5].

In this work, we attempt to solve the coating conundrum by developing rationally-designed metal-polymer composite coatings to increase effective thermal conductivity, thereby enabling thicker coatings for higher durability. Further, the proposed coatings have higher durability than their all-polymer ‘thick’ counterparts due to their higher elastic modulus [21].

The development of composite coatings through the addition of high thermal conductivity particles (e.g. metals) to low thermal conductivity matrices (e.g. polymers) has been studied widely for thermal-conductivity enhancement [22–26]. The interfacial resistances at the numerous polymer-metal interfaces [27–29], coupled with the inability to tailor the surface solid fraction make these approaches not suitable for enhancing dropwise condensa-

tion. Instead of randomly dispersed inclusions, we use metallic micro/nanostructures that are continuous from substrate to condensing surface to act as heat conducting ‘fins’ during dropwise condensation, with careful attention paid to the surface solid fraction of the composite to maintain low surface energy on the free (condensing) surface. We studied nanowire, inverse opal, and sintered sphere metallic structures filled with a range of hydrophobic polymers. To quantify the heat transfer performance, we analyzed the vapor-to-coolant and vapor-to-surface heat transfer coefficients of the composite coated flat surfaces having different wire/sphere diameters ($100 \text{ nm} < D < 10 \mu\text{m}$) and coating thickness ($10 \text{ nm} < t < 100 \mu\text{m}$). We used three-dimensional (3D), steady-state, finite element method (FEM) simulations with two distinct boundary conditions to obtain the coating’s effective thermal conductivity. By using two different boundary conditions (isothermal surfaces and convection at the walls) and by varying the interfacial metal fraction at the condensing surface, we demonstrate the importance of 3D heat spreading near the interfaces (coating-vapor and coating-substrate). We compare the obtained effective thermal conductivity of the coatings to analytical models based on effective medium theory [30] such as Maxwell [31] and Bruggeman [32] models, and previously studied opals models [33] to highlight the similarities and differences. Furthermore, to predict the wetting characteristics, we coupled our 3D FEM simulations to a unified model for contact angle hysteresis on heterogeneous surfaces [34]. Our wetting predictions identify the key tradeoff between low heat spreading resistance (high effective k , filmwise condensation) and low contact angle hysteresis (low effective k , dropwise condensation) on high and low surface metal fractions, respectively. Finally, we use our coupled models to predict the condensation heat transfer for the composite coatings as a function of metal volume fraction, metal interfacial solid fraction, and thickness.

2. Simulation Methods

2.1. Impact of Coating Properties on Overall Conductance

In order to observe the effects of the coating conundrum, and to obtain the thermal conductivity for the composite coating (k_{coating}) required to achieve greater durability, we analytically modelled a shell and tube heat exchanger with a hydrophobic coating. A non-specified fluid exchanges heat on the external shell-side while the cooling liquid flows on the internal tube-side. We used the model to study the effect of the coating’s thermal conductivity and thickness on the overall heat transfer coefficient (U) of the heat exchanger. We analyzed with the model of a single tube with a highly turbulent internal liquid flow, resulting in a fully developed turbulent heat transfer coefficient of $h_i = 20 \text{ kW}/(\text{m}^2 \cdot \text{K})$, and a typical dropwise steam condensation on the external tube surface with heat transfer coefficient of $h_e = 50 \text{ kW}/(\text{m}^2 \cdot \text{K})$, unless specified otherwise [35]. To demonstrate when the coating conundrum becomes important, we change the shell side (external tube surface) heat transfer coefficient (h_e) from $h_e = 10 \text{ W}/(\text{m}^2 \cdot \text{K})$ (natural convection of air) to $h_e = 100 \text{ kW}/(\text{m}^2 \cdot \text{K})$ (dropwise condensation of steam). A one-dimensional (1D) thermal resistance analysis is used [36]. Fig. 1 shows the overall decrease in U as a function of h_e for a variety of hydrophobic coating thicknesses, t . The overall decrease in U is computed relative to a case where the hydrophobic coating thermal resistance is arbitrarily set to zero (e.g. self-assembled monolayer) to represent the ideal case. We use three coating thermal conductivities with $k_{\text{coating}} = 0.1, 1, \text{ and } 10 \text{ W}/(\text{m} \cdot \text{K})$ representing state-of-the-art (SOA), achievable, and aspirational values, respectively. The results show that with SOA coatings ($k_{\text{coating}} = 0.1 \text{ W}/(\text{m} \cdot \text{K})$, Fig. 1(a)), utilizing a coating thickness, $t > 10 \mu\text{m}$, which will ensure reasonable durability to dropwise condensation of steam, results in an unacceptable 50% decrease in

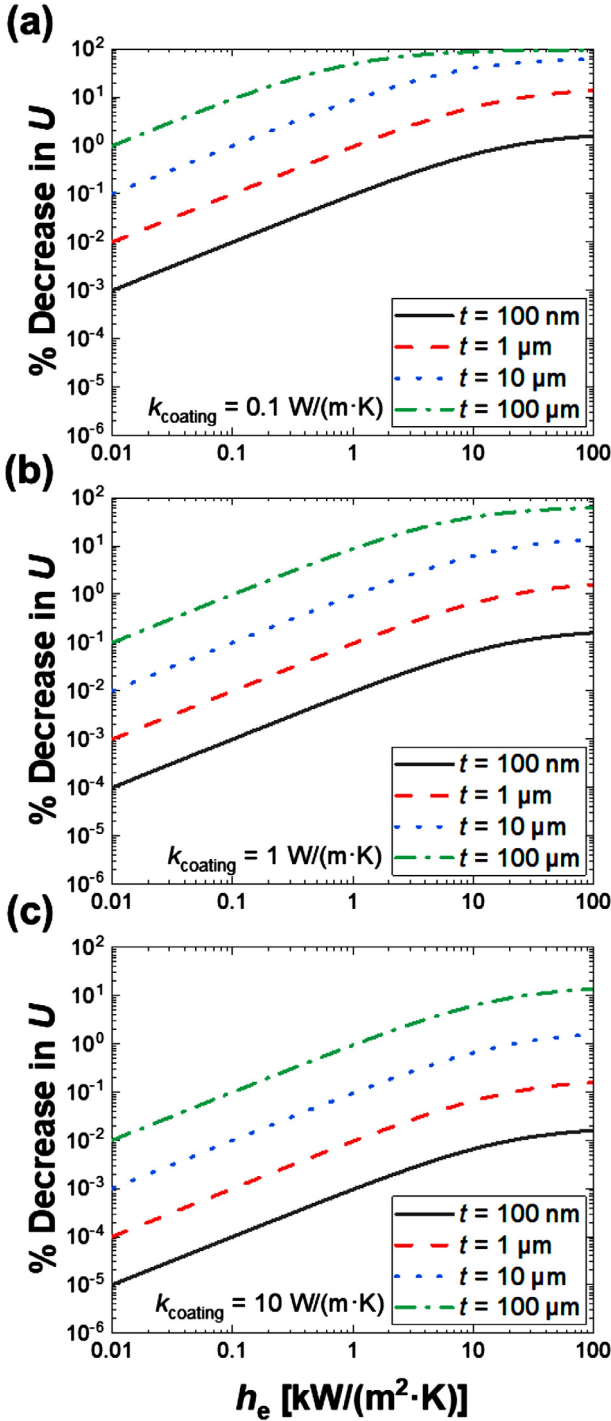


Fig. 1. Decrease in the overall heat transfer coefficient (U) of a fluid-to-fluid heat exchanger as a function of external heat transfer coefficient (h_e). The heat exchanger is coated on the exterior tube side with a hydrophobic coating having thickness (t) and coating thermal conductivity (k_{coating}) of (a) $0.1 \text{ W}/(\text{m} \cdot \text{K})$, (b) $1 \text{ W}/(\text{m} \cdot \text{K})$, and (c) $10 \text{ W}/(\text{m} \cdot \text{K})$. The model assumed an internal heat transfer coefficient of $h_i = 20 \text{ kW}/(\text{m}^2 \cdot \text{K})$, indicative of highly turbulent single phase water cooling. The percent decrease in U is referenced to the overall heat transfer coefficient without coating ($t = 0$). For heat transfer processes characterized by $h_e \gtrsim 10 \text{ kW}/(\text{m}^2 \cdot \text{K})$ (condensation or boiling), the decrease in U for hydrophobic coatings ($k_{\text{coating}} = 0.1 \text{ W}/(\text{m} \cdot \text{K})$, $t < 1 \mu\text{m}$) is appreciable ($> 10\%$).

U. If we were able to increase the coating thermal conductivity to $k_{\text{coating}} = 1 \text{ W}/(\text{m} \cdot \text{K})$, (Fig. 1(b)), the decrease in U could reduce to an acceptable level of a few percent. Increasing the conductivity further to $k_{\text{coating}} = 10 \text{ W}/(\text{m} \cdot \text{K})$, (Fig. 1(c)), reveals a negligible

coating thermal resistance and impact on U . Thus, the development of coatings with high effective thermal conductivity ($> 1 \text{ W}/(\text{m} \cdot \text{K})$) is desired in order to allow for the successful implementation of thicker and more durable hydrophobic coatings [37]. Note that for applications, with no phase change heat transfer (*i.e.* single-phase liquid or gas heat transfer, or natural convection), the resistance on the shell side (h_e) dominates any added resistance of a hydrophobic surface, enabling the use of thicker coating materials that are more durable without any concern for a decrease in U .

2.2. Metal-Polymer Composite Structured Surfaces

To enhance the thermal conductivity of the hydrophobic coatings, we utilize metal-polymer composite structured coatings, which consist of polymer-infilled structured (porous) metals. Here, three well-established metal structures are considered; micro- or nanowires [38–42], inverse opals [6,43–47], and sintered spheres [48,49]. The selection of the metal structures was due to: 1) the need for high thermal conductivity in the coating through-plane direction (normal to the coating surface), 2) the need for well-established manufacturing techniques that can be applied to base metals, 3) the ability to control the solid fraction of metal at the free condensing surface, which can enable low contact angle hysteresis to achieve stable dropletwise condensation, and 4) the ability to create arbitrarily thick coatings to enhance durability.

Schematics of the metal structures are shown in Fig. 2. After creating the porous structures, the voids are filled with a low-surface energy polymer to enable hydrophobicity on the outer surface. In the schematics of Fig. 2(a–c), the infilled material is not shown. Micro- or nanowires (Fig. 2(a)) having diameters, D , and heights, t , provide heat pathways through the coating. Metal wires can be fabricated with lithography or electrodeposition [40,50]. Metal inverse opals (Fig. 2(b)) having pore diameters, D , and neck diameters, d_n , also provide efficient heat pathways. Further, their porous structures can effectively hold hydrophobic polymer material to achieve dropletwise condensation by controlling surface solid fraction through opal termination location [47]. Inverse opal structures are fabricated by the electrodeposition of metals around a sacrificial template such as polystyrene spheres, followed by the dissolution of the sacrificial spheres [6,44]. Sintered metal structures having pore diameters, d_n , and spherical metal particles with diameters, D , are porous (Fig. 2(c)), enabling space for hydrophobic material, and can be sintered from compacted metal particles on arbitrary substrates [48]. Figs. 2(d–i) show top-view and side-view cross sections of the composite structures with polymer material shown as hatched regions. For the purposes of this study, we do not specify the polymeric material for the porous structure filling as many candidates exist (*e.g.* PMMA, PTFE, Parylene, Polyimide, PFDA, DVB [5,6,20,51,52]) which can satisfy both the required highly conformal filling of the entire pore structure, and the low contact angle hysteresis needed for dropletwise condensation of steam.

2.3. Simulation Framework

To compute the heat transfer rate through the structured composite coatings, we used the numerical simulation software COMSOL 5.3a. The steady-state 3D heat diffusion equation was solved for the different geometries with various dimensions, including variable nanowire, pore, or sphere size. Key parameters are all depicted in Figs 2 and are tabulated in Table 1. Briefly, for the micro- or nanowire structures, wire diameters having $D = 100 \text{ nm}$, $1 \mu\text{m}$, or $10 \mu\text{m}$, with different wire lengths (coating thickness) of $t = 10 \text{ nm}$, 100 nm , $1 \mu\text{m}$, $10 \mu\text{m}$, and $100 \mu\text{m}$ were simulated. For the inverse opal and the sintered sphere structures, different pore and sphere diameters were simulated including $D = 100 \text{ nm}$,

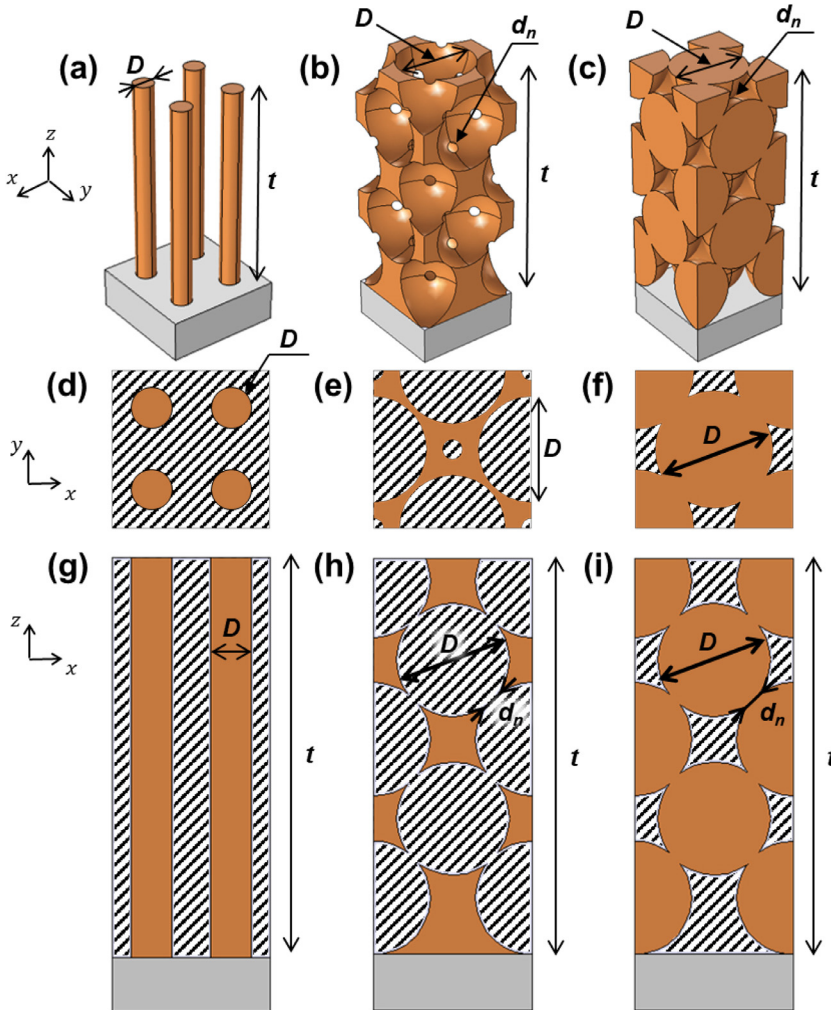


Fig. 2. Structured surfaces having potential for enhancing the effective thermal conductivity of composite coatings. 3D rendering of (a) micro/nanowires, (b) inverse opal structures, and (c) sintered metal structures grown on a metal substrate (gray base). Depictions (a-c) do not show the infilled hydrophobic material, which lends non-wetting function to the high thermal conductivity structures. Cross-sectional top view of (d) micro/nanowires, (e) inverse opal, and (f) sintered metal structures and cross-sectional side view of (g) micro/nanowires, (h) inverse opal, and (i) sintered metal structures. The infilled hydrophobic material is depicted as the hatched region, with the metal as solid orange.

Table 1

Parameters used for structures shown in Fig 2. For wires, D represents the diameter of cylindrical wires, while for inverse opals and sintered spheres, D represents the pore and metal particle diameters, respectively. The symbols d_n and t represent neck diameter and coating thickness, respectively.

Surface Structure	D [μm]	Neck diameter, d_n	Thickness, t
Wires	0.1, 1, 10	-	10 nm, 100 nm, 1 μm , 10 μm , 100 μm
Inverse opals	0.1, 1, 10	0.141 D , 0.199 D , 0.280 D , 0.341 D , 0.392 D	6.37 D < t < 7.29 D
Sintered spheres	0.1, 1, 10	0.141 D , 0.199 D , 0.280 D , 0.341 D , 0.392 D	6.37 D < t < 7.29 D

1 μm , and 10 μm , having different neck diameters $d_n = 0.141D$, $0.199D$, $0.280D$, $0.341D$, $0.392D$. We changed the neck diameters by changing the distance between two adjacent pores or spheres, calculated by $d_n = \sqrt{D^2 - d^2}$, where d represents the distance between two adjacent elements. The metal volume fraction was also dependent on the neck diameter. For inverse opals and sintered spheres, thicknesses ranged from $6.37D < t < 7.29D$. The thickness range was determined from the thickness of eleven layers of elements, and these were also independently investigated from the neck diameters. The inverse opals and sintered spheres had face-centered cubic (FCC) structures. We differentiated the top (outside) surface solid fraction, ϕ , or ratio of exposed metal to the total surface area, by slicing the top layer at various locations. The reduced thickness due to slicing was taken into account in all simulations,

hence the thicknesses are provided as a range depending on ϕ . The heat transfer is assumed to be through a flat surface, not through a curved tube surface. This assumption is valid because the characteristic length scale of the coating thickness ($\sim 1 \mu\text{m}$, Table 1) is several orders of magnitude smaller than the outer diameter characteristic length scale of practical tube geometries ($\sim 1 \text{ mm}$).

In order to ensure 1D heat transfer between internal and external surfaces, one or four adjacent unit cells, depending on size, were used with periodic boundary conditions on the side walls to emulate infinite lateral extent compared to the coating thickness (t). The physics-controlled mesh in COMSOL was used for the coating geometry with tetrahedral mesh and automatic refinement near interfaces. For simulations involving convective boundary conditions, a user-defined mesh was used due to the presence

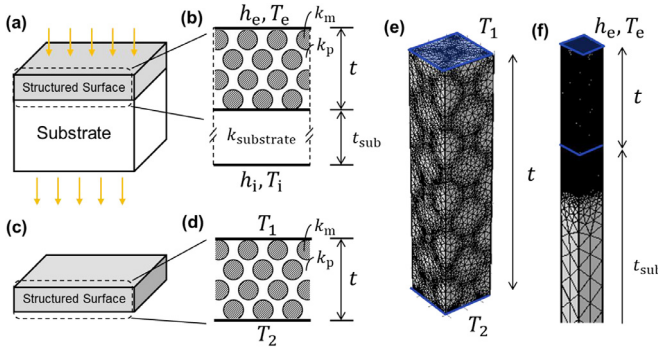


Fig. 3. Schematics of the two boundary conditions used to calculate heat transfer. The two boundary conditions were used for each geometry. (a, b) The structured surface coating is attached to a Cu substrate having thickness $t_{\text{sub}} = 1$ mm, $h_e = 50 \text{ kW}/(\text{m}^2 \cdot \text{K})$ and $h_i = 20 \text{ kW}/(\text{m}^2 \cdot \text{K})$. (c, d) The structured coating lies between two isothermal surfaces (T_1 and T_2). Exemplary corresponding mesh for an inverse opal simulation with (e) isothermal and (f) convective boundary conditions corresponding to (c, d) and (a, b) respectively. The overall heat transfer coefficients and effective thermal conductivities were calculated using following equations; (a, b) $U_h = q/A(T_e - T_i)$ and (c, d) $k_T = qt/A(T_1 - T_2)$.

of a much thicker substrate attached to the coating, making the physics-controlled mesh intractable. We adopted the geometric parameters (e.g. minimum element size, element growth rate, curvature factor, resolution of narrow regions) from the physics-controlled mesh in order to obtain analogous meshing for the structure, and coarser meshing for the substrate. The mesh was chosen to satisfy grid independence by examining different levels of physics-controlled mesh parameters. Figs. 3(e, f) show exemplary meshes generated for the inverse opal simulation with the described mesh settings. We used the stationary solver with a relative tolerance of 0.001 and generalized minimal residual method (GMRES) with residual tolerance of 0.01.

2.4. Simulation Boundary Conditions

Fig. 3 depicts the two different boundary conditions used for all simulations. First, in order to evaluate the thermal performance of the coating in a system (i.e. shell-and-tube condenser), the coating is assumed to be attached to a 1 mm thick copper (Cu) substrate with $k_{\text{sub}} = 400 \text{ W}/(\text{m} \cdot \text{K})$ (Fig. 3(a)) [53]. The sample is assumed to undergo forced convection with turbulent fluid flow on the inside surface, with condensation on the outside. The convection heat transfer coefficient is taken to be $h_i = 20 \text{ kW}/(\text{m}^2 \cdot \text{K})$ on the inside surface. The external heat transfer coefficient is $h_e = 50 \text{ kW}/(\text{m}^2 \cdot \text{K})$, typical for steady dropwise condensation of steam [54]. Although the simulation represents a physical phenomenon where individual condensate droplet length scales may approach the heterogeneous feature length scales (i.e. structure length scale D), the most important droplet sizes contributing to heat transfer (5 μm to 100 μm) [3,55,56] are at least one order of magnitude larger than the coating structure length scale for the majority of our simulations, hence an area-averaged convection heat transfer coefficient is used. This assumption may break down as the structure length scale approaches the individual droplet length scale (i.e. $D > 10 \mu\text{m}$), and is discussed further with results in the discussion section of the paper. Furthermore, individual droplets during condensation grow in a transient manner, resulting in rapid growth, coalescence, shedding, and re-nucleation, making the time averaged, steady, approximation of a spatially-averaged condensation heat transfer coefficient appropriate. In addition, past experimental studies have conclusively shown that the substrate material does not affect the condensation heat transfer coefficient, but it affects the thermal resistance of substrate itself and overall heat transfer coefficient

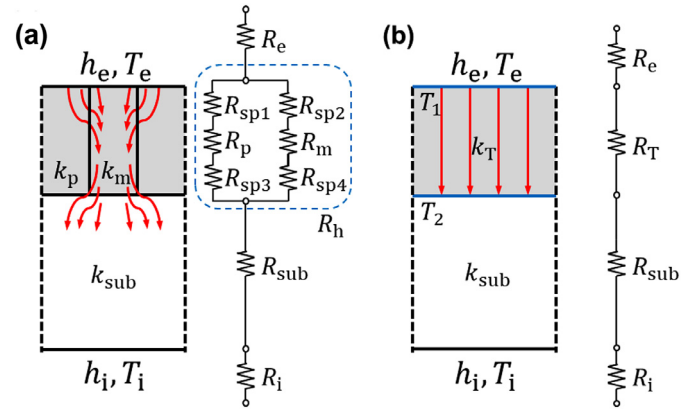


Fig. 4. Physically simplified representation of the steady-state spreading thermal resistances present for the (a) convective boundary condition and (b) isothermal boundary condition simulations. Note, the isothermal boundary simulations (b) do not capture spreading and hence the relevant thermal resistances are different. Thermal resistances R_e , $R_{\text{sp}1}$, $R_{\text{sp}2}$, R_p , R_m , $R_{\text{sp}3}$, $R_{\text{sp}4}$, R_{sub} , R_i , and R_T represent the external condensation heat transfer resistance, spreading resistance from metal to polymer at the condensation interface, polymer thermal resistance, metal thermal resistance, spreading resistance from polymer to metal at the substrate interface, spreading resistance from metal to polymer at the substrate interface, substrate thermal resistance, internal convection heat transfer resistance, and total heat transfer resistance through a coating as an effective medium, respectively.

[5,57,58], hence the use of a fixed condensation heat transfer coefficient on the heterogeneous surface is appropriate.

As a second, independent, and more convenient boundary condition, both sides of the coatings are set to be isothermal surfaces at temperatures T_1 and T_2 (Fig. 3(b)). The utilization of isothermal surfaces is consistent with the widely-used definition of effective thermal conductivity [59]. In our case, both the metal and polymer at the surfaces are assumed to be at the same temperature. The main reason for using separate isothermal and convective boundary conditions is due to the fact that conventionally used isothermal boundary condition may not capture the effects of 3D heat spreading near the interfaces of interest, which may be appreciable (Fig. 4). Given the highly inhomogeneous thermal conductivity distribution of the composite coatings, spreading effects must be considered. When the conventional isothermal boundary condition is used, the heat path is always assumed to be parallel, with planes having infinite lateral conductance characteristic of 1D heat conduction. Hence, the coating can be described as a single monolithic component with an effective thermal conductivity k_T . However, the actual coating attached to the substrate undergoes 3D conduction due to material inhomogeneity, which leads to additional thermal resistance. These additional terms are characterized as thermal spreading resistances, and are captured by the inclusion of convective boundary conditions. Fig. 4 depicts the difference of the thermal resistances under two separate boundary conditions.

It is important to note, for the simulations reported here, the thermal conductivities of the metal and hydrophobic material phases were assumed to be $k_m = 400 \text{ W}/(\text{m} \cdot \text{K})$ and $k_p = 0.1 \text{ W}/(\text{m} \cdot \text{K})$, respectively, typical for Cu and hydrophobic polymers [53,60]. Interfacial thermal resistances at the metal-polymer interfaces were not considered due to the macroscopic scale of the structures used for the majority of our simulations. Furthermore, the typical resistance values for a metal-polymer interfaces are on the order of 10^{-6} to $10^{-8} \text{ (m}^2 \cdot \text{K})/\text{W}$ [61,62], much lower when compared to the resistance of the thinnest composite coating $\sim 10^{-4} \text{ (m}^2 \cdot \text{K})/\text{W}$ (Fig. 5). To verify our assumption, baseline simulations show that assuming an interfacial thermal resistance of $10^{-7} \text{ (m}^2 \cdot \text{K})/\text{W}$ results in a 4.1 % decrease in the overall thermal resistance using the thickest inverse opal coating. For thinner

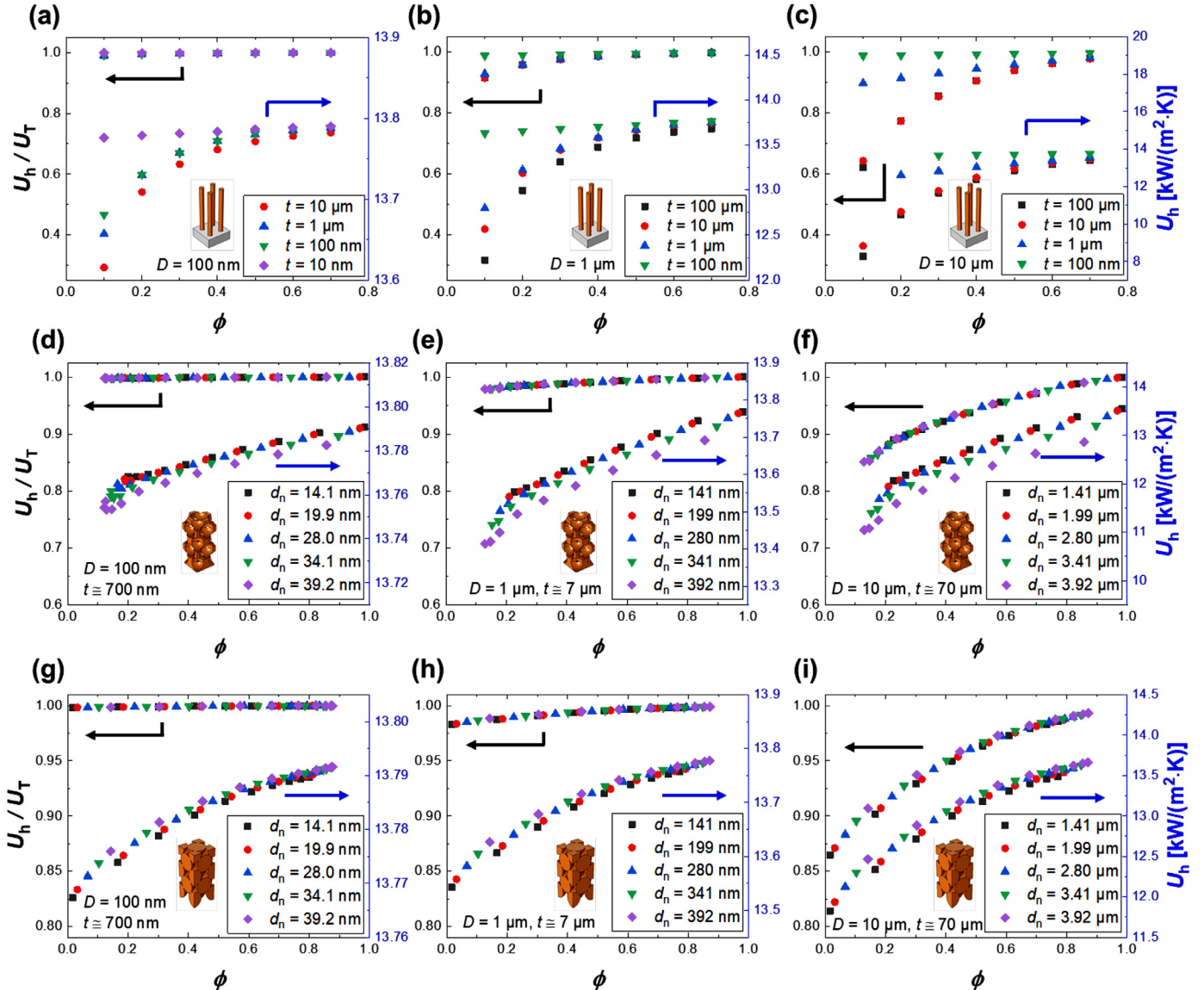


Fig. 5. Ratio of the convection (U_h) and isothermal boundary condition (U_T) overall heat transfer coefficients (left black axis) as a function of ϕ and t for wire diameters D of (a) 100 nm, (b) 1 μm , and (c) 10 μm . Inset: Schematic of wire geometry not showing the hydrophobic filler. For wire structures, $\phi = (\pi D^2)/(4L^2)$. Results in (d-f) represent inverse opal structures having varying d_n with D of (d) 100 nm, (e) 1 μm , and (f) 10 μm . Inset: Schematic of the inverse opal geometry not showing the hydrophobic filler. Results in (g-i) represent sintered sphere structures having varying d_n with D of (g) 100 nm, (h) 1 μm , and (i) 10 μm . Inset: Schematic of sintered sphere geometry not showing the hydrophobic filler. The right blue axis for all figures represents the dimensional U_h . Here, U_T was calculated using summation of thermal resistances; $U_T^{-1} = h_i^{-1} + t_{\text{sub}}k_{\text{sub}}^{-1} + tk_T^{-1} + h_e^{-1}$. The coating thermal conductivity k_T was determined based on the simulation of the same structured surface composite between two isothermal surfaces, in agreement with currently accepted definition of effective thermal conductivity.

coatings, the utilization of the interfacial resistance results in < 1 % difference compared to simulations assuming negligible interfacial resistance.

2.5. Post-Processing of Simulations Results

We first computed the total heat transfer rate (q) through the composite coating, and then determined the overall heat transfer coefficient (U) of coating-substrate system and the effective thermal conductivity (k). Two sets of overall heat transfer coefficients and effective thermal conductivities were obtained based on the two distinct boundary conditions. We denote the overall fluid-to-fluid heat transfer coefficient calculated from the convection boundary condition simulation (Fig. 3(a, b)) as U_h :

$$U_h = \frac{q}{A(T_e - T_i)}, \quad (1)$$

where q is the total heat transfer rate through the surface, A is the projected area of the surface, T_e and T_i are the outer and inner fluid temperatures (Fig. 3(b)), respectively. A 1D series thermal resistance analysis was conducted to calculate the effective thermal conductivity (k_h) obtained from simulations using convection boundary conditions of the composite structured surface (Fig. 3(a, b)):

$$k_h = \frac{t}{\frac{1}{U_h} - \frac{1}{h_i} - \frac{t_{\text{sub}}}{k_{\text{sub}}} - \frac{1}{h_e}}. \quad (2)$$

For the isothermal surface boundary condition (Fig. 3(c, d)), the effective thermal conductivity k_T , is calculated as:

$$k_T = \frac{qt}{A(T_1 - T_2)}, \quad (3)$$

where T_1 and T_2 are the isothermal surface temperatures (Fig. 3(d)), respectively. The effective thermal conductivity (k_T ,

[Eq. 3](#)) was used in a similar 1D thermal resistance analysis to compute the overall heat transfer coefficient (U_T) for the isothermal boundary scenario [36]:

$$U_T = \frac{1}{\frac{1}{h_i} + \frac{t_{sub}}{k_{sub}} + \frac{t}{k_T} + \frac{1}{h_e}} \quad (4)$$

3. Results and Discussion

[Fig. 5](#) shows the ratio of the heat transfer coefficients (U_h/U_T) as well as the overall heat transfer coefficient U_h (right blue axis) as a function of the surface metal solid fraction (ϕ) for all structures. The solid fraction of the metal micro/nanowires ([Fig. 5\(a, b, c\)](#)) was varied by controlling the center-to-center spacing of the wires. The wire structured surface showed that at small wire diameters ([Fig. 5\(a\)](#), $D=100$ nm), the difference between U_h and U_T is negligible. As ϕ decreases, the overall heat transfer coefficient decreased due to fewer parallel heat transfer pathways. The negligible difference between the two results is due to the fact that at small length scales ($D=100$ nm), the spreading resistance near the nanowire-surface interface ([Fig. 4\(a\)](#)) becomes negligible compared to other thermal resistances in the system. This makes the analysis using convective boundary conditions ([Fig. 3\(a, b\)](#)) unnecessary, enabling the use of the well-established isothermal method ([Fig. 3\(c, d\)](#)) to compute the effective transport properties. However, as the metal wire dimensions increased from $D=100$ nm ([Fig. 5\(a\)](#)), to $D=1\mu\text{m}$ ([Fig. 5\(b\)](#)), to $D=10\mu\text{m}$ ([Fig. 5\(c\)](#)), the discrepancy between the two boundary conditions increased. At large wire diameters ($D=10\mu\text{m}$, [Fig. 5\(c\)](#)), the isothermal method overestimated heat transfer by as much as 50% at low metal solid fractions ($\phi < 0.2$). The higher calculated overall heat transfer coefficient using the isothermal case ([Eq. 4](#)) is due to the inability to resolve the 3D heat spreading resistance near the free surfaces, in essence assuming infinite lateral conductance ([Fig. 4\(b\)](#)).

In addition to the effect of ϕ , cases where t was small (i.e. $t=100$ nm) showed little variance between the two boundary conditions. The negligible difference in the thin coating limit was due to the dominance of the polymer thermal resistance when compared to other resistances in the coating, including metal conduction and 3D heat spreading.

Inverse opals ([Fig. 5\(d, e, f\)](#)) and sintered spheres ([Fig. 5\(g, h, i\)](#)) showed similar trends as the wire structures, indicating the inability to resolve important and sometimes dominant 3D heat spreading resistance near the free boundaries when the isothermal boundary condition is used. The results point to the need for full 3D simulations using convective heat transfer coefficients if structures having low ϕ are to be utilized, as proposed here due to wetting considerations. At high metal solid fractions ($\phi > 0.5$), the discrepancy between the two boundary conditions fades, and utilization of the computationally simple isothermal method is appropriate and favored.

[Fig. 5](#) reveals that the highest overall heat transfer coefficients were attained in the inverse opal and sintered sphere structures. The higher overall conductance stems from the higher lateral interconnectedness, allowing for effective lateral heat transfer. The sintered sphere structures showed higher overall conductance when compared to inverse opals due to their higher metal volume fraction. Inverse opals are ideal for liquid propagation studies where low metal volume fractions are needed for capillary pressure generation and high flow rates due to evaporation [6,44,47,63]. In our simulations, the ability to fill the pores with polymer is a key enabler for attaining a higher effective thermal conductivity of the coating. However, the more important metric to consider is ϕ due to its important impact on wettability.

[Fig. 6](#) shows the ratio of the effective thermal conductivity calculated from the convective boundary conditions (k_h , [Eq. 2](#), [Fig. 3\(a,](#)

b)) to that from isothermal boundary condition (k_T , [Eq. 3](#), [Fig. 3\(c, d\)](#)) as a function of ϕ for all of the considered structures. Contrary to the overall heat transfer coefficient results ([Fig. 5](#)), the wire structures of small wire diameters ([Fig. 6\(a\)](#), $D=100$ nm), show the largest difference between k_T and k_h . Although the case with $D=100$ nm showed negligible difference in the overall heat transfer coefficient ratio (U_h/U_T , [Fig. 5\(a\)](#)), k_h was three orders of magnitude smaller than k_T . The large effective thermal conductivity discrepancy stems from the assumption of infinite lateral conductance for the isothermal case. In reality, for thin coatings ($t=10$ nm), heat spreading is difficult due to spatial constraints, and hence the boundaries are highly non-isothermal. Conversely, for thicker coatings ($t=10\mu\text{m}$), k_h/k_T approaches unity (≈ 0.7).

It is important to note that although $k_h/k_T \rightarrow 1$ for thicker coatings (e.g. $t=10\mu\text{m}$), the coating plays a more important role in the overall conductance calculation as thicker coatings have higher heat transfer resistance. [Fig. 5](#) demonstrates this, showing that U_h/U_T for thicker coatings significantly deviates from 1, and has a sharp decrease in overall conductance ratio of the two boundary conditions for lower ϕ . The lower resistance of thinner coatings results in $U_h/U_T \rightarrow 1$, while $k_h/k_T \rightarrow 10^{-3}$.

Inverse opals ([Fig. 6\(d, e, f\)](#)) and sintered spheres ([Fig. 6\(g, h, i\)](#)) show the same trends as the wire structures, with higher convergence at higher ϕ . The reason for convergence was due to the lateral interconnectedness of the inverse opal and sintered sphere structures, enabling effective 3D heat spreading and lower discrepancy between the convective and isothermal boundary condition methods. For $\phi \ll 1$, $k_h/k_T \ll 1$, indicating the importance of resolving 3D heat spreading at boundaries.

For the inverse opals and sintered spheres, increasing the neck diameter (d_n) resulted in a higher and lower k_h/k_T , respectively, for any given ϕ . The reduction or enhancement obtained from larger d_n in inverse opal or sintered sphere structures, respectively, disproportionately affected the heat transfer results for the isothermal boundary condition.

3.1. Effective Thermal Conductivity

[Fig. 7](#) shows k_h ([Eq. 2](#), [Fig. 3\(a, b\)](#)) as a function of ϕ for all of the considered structures. The wire structures showed that at small wire diameters ([Fig. 7\(a\)](#), $D=100$ nm), thin coatings ($t=10$ nm) had the lowest k_h due to the significant spreading resistance near the free surfaces. Although the $D=100$ nm case showed the highest overall heat transfer coefficient of $U_h \approx 13.8 \text{ kW}/(\text{m}^2\cdot\text{K})$ for the thinnest coating of $t=10$ nm, the coating plays a more important role in the overall heat transfer coefficient as t increases, due to thicker coatings having higher heat transfer resistance. Thick wire structure composite coatings ($t=10\mu\text{m}$) showed the highest k_h due to the greater ability to spread heat. In particular, $\phi=0.1$ demonstrated $k_h = 10 \text{ W}/(\text{m}\cdot\text{K})$.

It is important to note that the effective thermal conductivity is thickness dependent when using the convective boundary condition, which is not intuitive. Heat spreading is a 3D phenomenon, not a 1D (thickness independent) behavior. For thicker coatings, heat spreading effects are less dominant as the boundary effects become less pronounced compared to bulk conduction, therefore the disagreement between two boundary conditions vanishes.

For wire structures having larger D ([Fig. 7\(b, c\)](#)), the same trends were valid with a general observation of decreased k_h as D increased. The lower k_h for larger D stems from the larger spreading resistance at larger length scales (for the same geometry). The results indicate that for metal wires, the use of nanowires as opposed to microwires is beneficial due to the elimination of heat spreading near the interfaces. For example, nanowires and microwires with same solid fraction have identical parallel components of thermal resistance. However, lateral spreading resistance

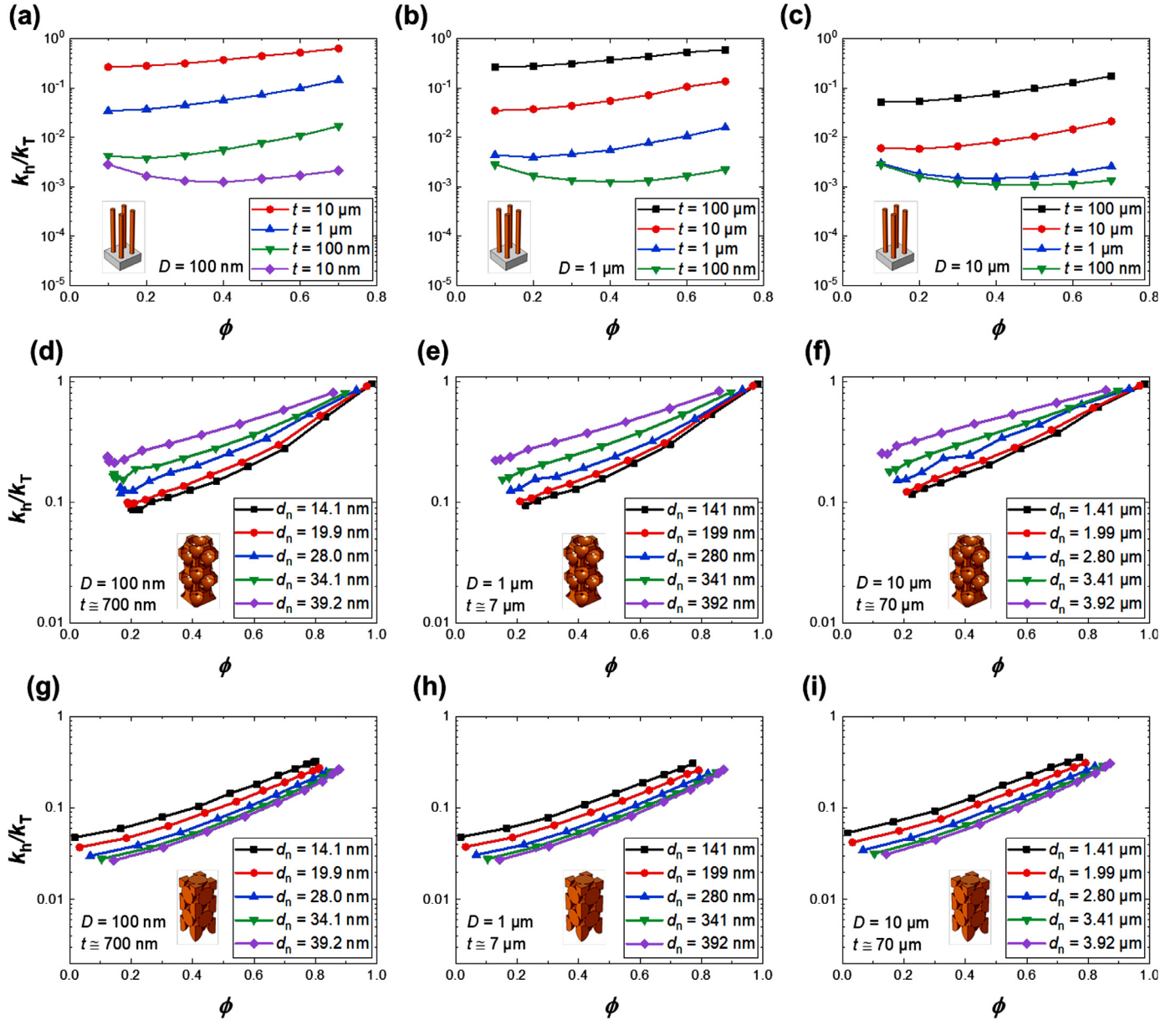


Fig. 6. Ratio of the convection (k_h) to the isothermal (k_T) boundary condition thermal conductivity as a function of ϕ and t for wire diameters D of (a) 100 nm, (b) 1 μm , and (c) 10 μm . Inset: Schematic of wire geometry not showing the hydrophobic filler. Results in (d-f) represent inverse opal structures having varying d_n with D of (d) 100 nm, (e) 1 μm , and (f) 10 μm . Inset: Schematic of the inverse opal geometry not showing the hydrophobic filler. Results in (g-i) represent sintered sphere structures having varying d_n with D of (g) 100 nm, (h) 1 μm , and (i) 10 μm . Inset: Schematic of sintered sphere geometry not showing the hydrophobic filler. Here, k_h was calculated by $tk_h^{-1} = U_h^{-1} - h_i^{-1} - t_{\text{sub}}k_{\text{sub}}^{-1} - h_e^{-1}$.

differs because they have different lateral distances for heat flow. Microwires have longer lateral distances for heat flow (spreading) compared to nanowires, hence the microwires have reduced effective thermal conductivity in the through-plane direction.

The inverse opals (Fig. 7(d, e, f)) and sintered spheres (Fig. 7(g, h, i)) show the same qualitative trends as the wire structures. Lower ϕ resulted in lower k_h . Increasing d_n resulted in lower and higher k_h for the inverse opal and sintered sphere structures, respectively. Because d_n for inverse opals characterizes the size of voids between metals while d_n in sintered spheres characterizes the size of contacts between metals, the opposing trends in k_h are expected. Larger d_n for inverse opals results in lower interconnectivity of the metal structure, and lower overall heat trans-

port. However, larger d_n for sintered spheres results in higher interconnectivity of the metal, and better heat transport. It is important to note that the range of neck diameter is different for the inverse opal and sintered sphere structures in Fig. 7(d-i). For sintered spheres, the surface metal fraction near zero could easily be achieved with small neck diameters, while inverse opals needed larger neck diameters to achieve the same surface metal fraction. Because of this, a wider range of neck diameters was simulated for the inverse opal structures. The results showed that inverse opal composite structures with $\phi=0.2$ and $d_n=14.1$ nm have the potential to achieve $k_h \approx 6 \text{ W}/(\text{m}\cdot\text{K})$. Furthermore, sintered sphere composite structures with $\phi=0.1$ and $d_n=14.1$ nm have the potential to achieve $k_h \approx 5.2 \text{ W}/(\text{m}\cdot\text{K})$.

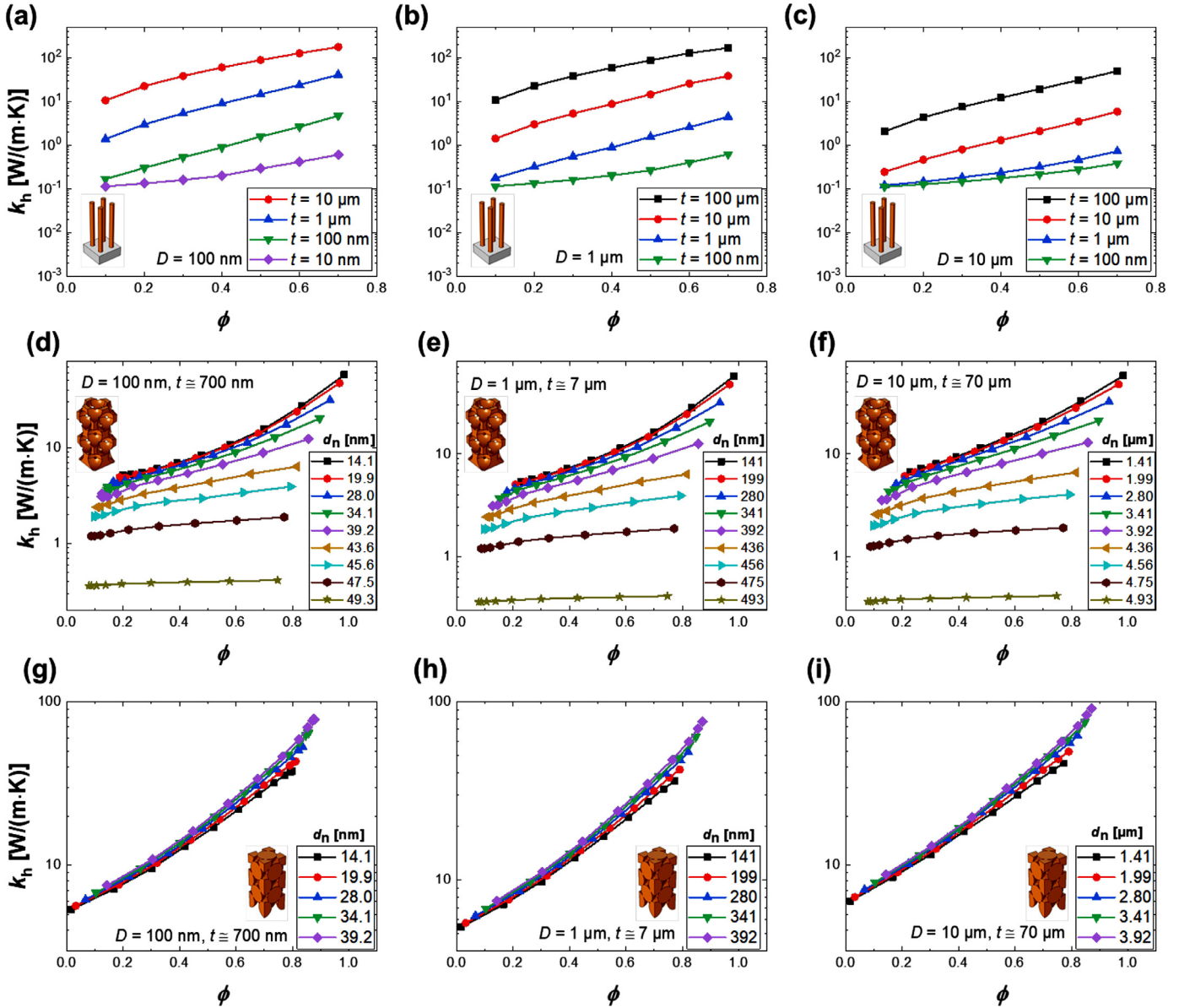


Fig. 7. Effective thermal conductivity of the composite structured surfaces (k_h) obtained from simulations as a function of ϕ and t for wire diameters D of (a) 100 nm, (b) 1 μm , and (c) 10 μm . Inset: Schematic of wire geometry not showing the hydrophobic filler. Results in (d-f) represent inverse opal structures having varying d_n with D of (d) 100 nm, (e) 1 μm , and (f) 10 μm . Inset: Schematic of the inverse opal geometry not showing the hydrophobic filler. Results in (g-i) represent sintered sphere structures having varying d_n with D of (g) 100 nm, (h) 1 μm , and (i) 10 μm . Inset: Schematic of sintered sphere geometry not showing the hydrophobic filler.

3.2. Comparison with Theory

We compare our computational results with previously developed theoretical models to compute the effective thermal conductivity of composite materials. We considered the effective medium theory (EMT) [30] and the parallel resistance model [64,65]. Briefly, the parallel model assumes that heat flows through the composite structure, consisting of filler material oriented parallelly along the direction of heat flow, with no heat spreading between the differing phases.

$$k_{\text{parallel}} = k_m \psi + k_p (1 - \psi), \quad (5)$$

where ψ is the volume fraction of metal in the composite coating. Note that $\psi \neq \phi$, and ϕ represents the surface solid fraction.

The effective medium theory (EMT) approximates the effective property of a composite using only the properties of the constituents and their volume fractions. Among the well-known EMT

approximations, we consider Maxwell's and Bruggeman's model [66]. The Maxwell model assumes that spherical metal particles are dispersed randomly in a homogeneous polymer matrix. It also assumes no interaction between particles, thus working well for low volume fractions, or dilute mixtures [31]. To overcome this limitation, Bruggeman developed a model which assumes a random distribution of both phases but considers interactions among particles [32]. The effective thermal conductivity can be represented using the following equations respectively:

$$k_{\text{Maxwell}} = k_p \frac{k_m + 2k_p + 2\psi(k_m - k_p)}{k_m + 2k_p - \psi(k_m - k_p)}, \quad (6)$$

$$\psi \frac{k_m - k_{\text{Bruggeman}}}{k_m + 2k_{\text{Bruggeman}}} + (1 - \psi) \frac{k_p - k_{\text{Bruggeman}}}{k_p + 2k_{\text{Bruggeman}}} = 0. \quad (7)$$

We only considered comparison with k_T as the aforementioned theories have all been developed using the isothermal boundary approach. Fig. 8 shows k_T of our wire (black squares),

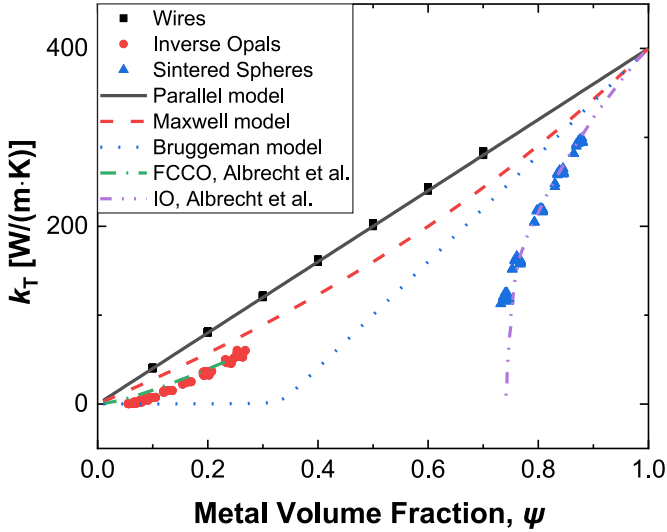


Fig. 8. Calculated effective thermal conductivity (k_T) of the composite coating using the parallel model (solid line), EMT (Maxwell model dashed line, Bruggeman model dotted line), and boundary-integral method (FCCO dash-single dotted line, IO dash-double dotted line) [33] as a function of metal volume fraction (ψ). Boundary integral method calculations are based on the void pores ($k_p = 0$) instead of polymer ($k_p = 0.1 \text{ W}/(\text{m}\cdot\text{K})$). Also plotted are the simulation results for k_T with isothermal boundary conditions for the three structures. Wires show good agreement with the parallel model, while the two other structures show good agreement with the boundary-integral solutions.

inverse opal (red circles), and sintered sphere (blue triangles) composite structures, along with the calculations based on the parallel model (solid black line), EMT (Maxwell model with dashed red line, Bruggeman model with dotted blue line), and boundary-integral method (FCC opals with green dash-dot line, inverse opals with purple dash-dot line) [33].

The effective thermal conductivity of the three geometries considered here were plotted together in Fig. 8 to study the trends. Wire structures showed good agreement with the parallel model due to the parallel nature of heat transport in the isolated wire structures. Furthermore, the metal and polymer phases are not reasonably randomized or mixed as is required for accuracy using EMT. Maxwell's model assumes no percolation, while the Bruggeman model has a percolation threshold of $\sim 33\%$ [67], as evident from Fig. 8. Ideally, the percolation threshold and its exponents are dependent on the size and shape of the structures [64,68]. The thermal conductivity of inverse opal structures lies between the Maxwell and Bruggeman models, but closely follows the trend of the Maxwell model, indicating low percolation threshold (< 0.1), consistent with inverse FCC structures. The thermal conductivity of sintered spheres lie to the far right of the Bruggeman model, indicating a higher percolation threshold (~ 0.74), consistent with FCC's maximum volume fraction. The discrepancy between EMT models and data arises due to the difference in shape, size, and the fact that the secondary phase is not randomized in comparison to the EMT models [68–70]. The boundary-integral method solutions agree well with the computed thermal conductivity for inverse opals and sintered spheres, which further validates our simulations (Fig. 8). However, for the composite structures studied here, EMT and boundary-integral methods cannot be used to predict the effective thermal conductivity under convective conditions (k_h), providing rationale for the use of 3D finite element simulations.

3.3. Wettability

Although a wide range of ϕ was used in our simulations, ϕ needs to be carefully considered to ensure dropwise condensation.

Due to the high surface energy ($> 1 \text{ J/m}^2$) of clean metal oxides [71,72], condensate water will wet the exposed metal structures at the top of the coating. Hence, ϕ should be smaller than a certain critical value in order to ensure stable dropwise condensation and global hydrophobicity.

To model the composite coating surface wettability, we utilized a previously developed model capable of analytically computing the contact angle hysteresis on chemically heterogeneous smooth surfaces. The thermodynamic energy approach for contact line distortion and contact line pinning is accounted for in the model, which has been experimentally validated for a wide range of solid fractions with circular defects [34]. Due to the nature of the advancing contact line, the presence of high surface energy defects (exposed metal having intrinsic advancing contact angle of $\theta_{A,m}$) on the low surface energy background (polymer having intrinsic advancing contact angle $\theta_{A,p}$) does not change the intrinsic advancing contact angle when the surface fraction of defects is low enough that defects do not interconnect with each other. Hence, the composite structured coating's advancing contact angle (θ_A) will be equivalent to the polymer intrinsic contact angle:

$$\cos \theta_A = \cos \theta_{A,p} . \quad (8)$$

The receding contact angle on the heterogeneous surface is determined by considering the fraction of distorted contact line during contact line motion (f_{\max}) [34]:

$$\cos \theta_R = f_{\max} \cos \theta_{R,m} + (1 - f_{\max}) \cos \theta_{R,p} . \quad (9)$$

For our model, $f_{\max} = D/L$, where D is the diameter and L is center-to-center distance of adjacent defects. The terms $\theta_{R,m}$ and $\theta_{R,p}$ represent the intrinsic receding contact angles of the hydrophilic metal structure, and the hydrophobic polymer, respectively. For the case of hydrophobic defects, the equations invert and the following equations govern wettability:

$$\cos \theta_A = f_{\max} \cos \theta_{A,p} + (1 - f_{\max}) \cos \theta_{A,m}, \quad (10)$$

$$\cos \theta_R = \cos \theta_{R,m} . \quad (11)$$

Fig. 8 shows the composite surface θ_A and θ_R as a function of ϕ . When considering the shape of the metallic phase at the surface of the coating, wires and sintered spheres act as circular hydrophilic defects (Fig. 9(a, b) inset). Conversely, inverse opals composite coatings have the hydrophobic polymer as the circular hydrophobic defect (Fig. 9(c, d)). For all calculations, the intrinsic advancing and receding contact angles of the hydrophilic metal oxide (CuO) were assumed to be $\theta_{A,m} = 80^\circ$ and $\theta_{R,m} = 0^\circ$ [72–74]. The intrinsic contact angles of the hydrophobic polymer were assumed to be $\theta_{A,p} = 125^\circ$ and $\theta_{R,p} = 115^\circ$, typical for hydrophobic polymer materials (Fig. 9(a, c)) [3]. To gain an appreciation of the effect of contact angle hysteresis ($\Delta\theta = \theta_A - \theta_R$), simulations were also conducted for a polymer having ultra-low $\Delta\theta = 1^\circ$ (Fig. 9(b, d)), with $\theta_{A,p} = 120^\circ$ and $\theta_{R,p} = 119^\circ$, representative of lubricant infused surfaces [75–79], or covalently attached liquids [80].

Recent work has revealed that the key to attaining stable dropwise condensation on smooth surfaces lies in minimizing the contact angle hysteresis [81–83]. To determine the regime of dropwise condensation as a function of ϕ , we used the previously developed regime map which related the condensation mode to contact angle hysteresis [82]. Briefly, the regime map revealed that for coatings having $\theta_A = 125^\circ$ or $\theta_A = 120^\circ$, the required contact angle hysteresis to achieve dropwise condensation must be lower than 56° or 54° , respectively. The results showed that for metallic wires and sintered spheres, stable dropwise condensation can be achieved if $\phi < 0.24$ ($\theta_{A,p}/\theta_{R,p} = 125^\circ/115^\circ$), or $\phi < 0.29$ ($\theta_{A,p}/\theta_{R,p} = 120^\circ/119^\circ$). For inverse opals, dropwise condensation occurs for $\phi < 0.12$ ($\theta_{A,p}/\theta_{R,p} = 125^\circ/115^\circ$) or $\phi < 0.13$ ($\theta_{A,p}/\theta_{R,p} = 120^\circ/119^\circ$).

For all wettability results, minimization of $\Delta\theta$ of the polymer phase, along with minimization of ϕ resulted in the lowest

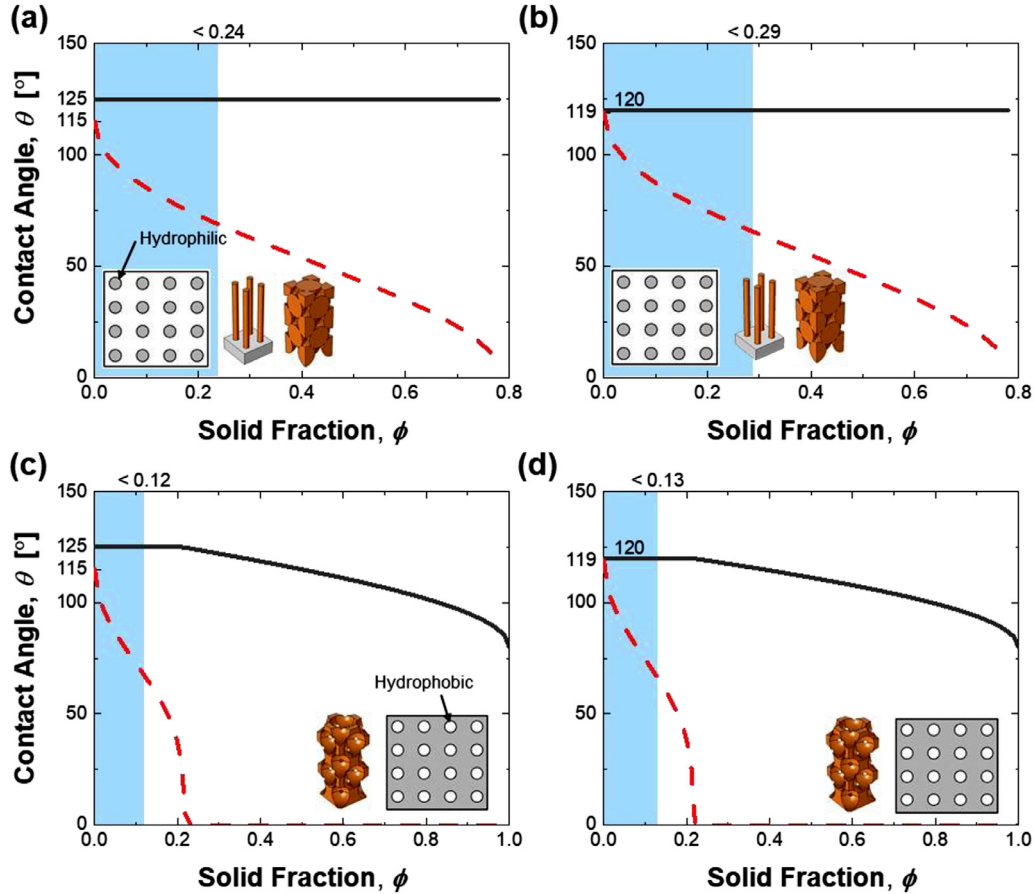


Fig. 9. Advancing (black solid lines) and receding (red dashed lines) contact angles as a function of ϕ for wire and sintered sphere composite structures having $D = 10 \mu\text{m}$ and hydrophobic filler materials with (a) $\theta_{A,p} = 125^\circ$ and $\theta_{R,p} = 115^\circ$ or (b) $\theta_{A,p} = 120^\circ$ and $\theta_{R,p} = 119^\circ$. For the wires and sintered spheres, the metal exposed on top is represented with hydrophilic circular defects with $\theta_{A,m} = 80^\circ$ and $\theta_{R,m} = 0^\circ$. Inset: Schematics of the wire and sintered sphere geometries not showing the hydrophobic filler. Advancing and receding contact angle behavior on inverse opal composite structures having hydrophobic filler materials with (c) $\theta_{A,p} = 125^\circ$ and $\theta_{R,p} = 115^\circ$ or (d) $\theta_{A,p} = 120^\circ$ and $\theta_{R,p} = 119^\circ$. Inset: Schematic of the inverse opal structure geometry not showing the hydrophobic filler. For inverse opals, the hydrophobic material exposed on top is represented with hydrophobic defects. The surrounding metal has $\theta_{A,m} = 80^\circ$ and $\theta_{R,m} = 0^\circ$. The shaded blue region represents surface structure designs having dropwise condensation.

composite structured surface $\Delta\theta$, and hence dropwise condensation stability. The shaded blue regions in Fig. 9 represents the regimes where stable dropwise condensation will be achieved on the composite coatings. Thus, we now focus our heat transfer analysis on the computed surface metal solid fraction ranges that ensures dropwise condensation stability to quantify the potential enhancement of utilizing composite coatings.

3.4. Discussion

Figures 10(a), (c), and (d) show the overall heat transfer coefficient (U_h) as a function of ϕ , bounded by the range which will ensure stable dropwise condensation (Fig. 9). Due to the importance of 3D heat spreading, the simulations utilized the convective boundary conditions. Fig. 10(b) shows U_h as a function of t for $\phi = 0.1$, and variable wire diameter D . In order to ensure better coating durability, we set the desired composite coating thickness to be $t > 10 \mu\text{m}$ [3]. The sintered sphere structured surfaces achieve the highest U_h , regardless of t . The good performance of sintered spheres is attributed to their ability to achieve a simultaneous high ψ with a low ϕ . However, the sintered sphere geometry is also most sensitive to damage or polymer erosion, as any removal of the polymer fill layer will result in a rapid increase in ϕ , and transition to filmwise condensation. Inverse opals on the other hand have relatively low ψ and maintain lower ϕ even after polymer removal. Wires are also able to maintain a constant metal

surface fraction ϕ with polymer removal. In essence, the inclusion of a structured surface metallic backbone may pose similar problems as those experienced with current dropwise condensing coatings, where the metal structure at the very top of the coating becomes the ‘new’ substrate. Although possible, we envision polymer erosion at the top surface to not be a problem due to the much thicker coating morphologies enabled with the current approach, coupled with the highly porous network of metallic backbone capable of holding the polymer material. The addition of the metallic backbone will in fact increase the Young’s modulus of the coating, resulting in even greater durability when compared to an equivalent all-polymer coating [84]. It is important to note, although predicting the exact quantitative relationship between coating thickness and durability is difficult, thicker coatings have been shown to extend the lifetime of dropwise condensation. For example, polytetrafluoroethylene (PTFE) layers have been reported to be sufficiently durable when the thickness of the coating is approximately 20–30 μm [3,5]. In this case, the thermal resistance of the PTFE layer was too high to show any benefit of dropwise condensation on the overall heat transfer. Furthermore, organic coatings have been shown to be durable for 2 years with 1 μm thickness [85]. One of the main mechanism for coating degradation is blister formation, thus, the durability of a coating highly depends on its thickness. The mechanics of blister formation and coating stress generation during blister growth results in thicker coatings having higher resistance to blistering, which increases durability [84].

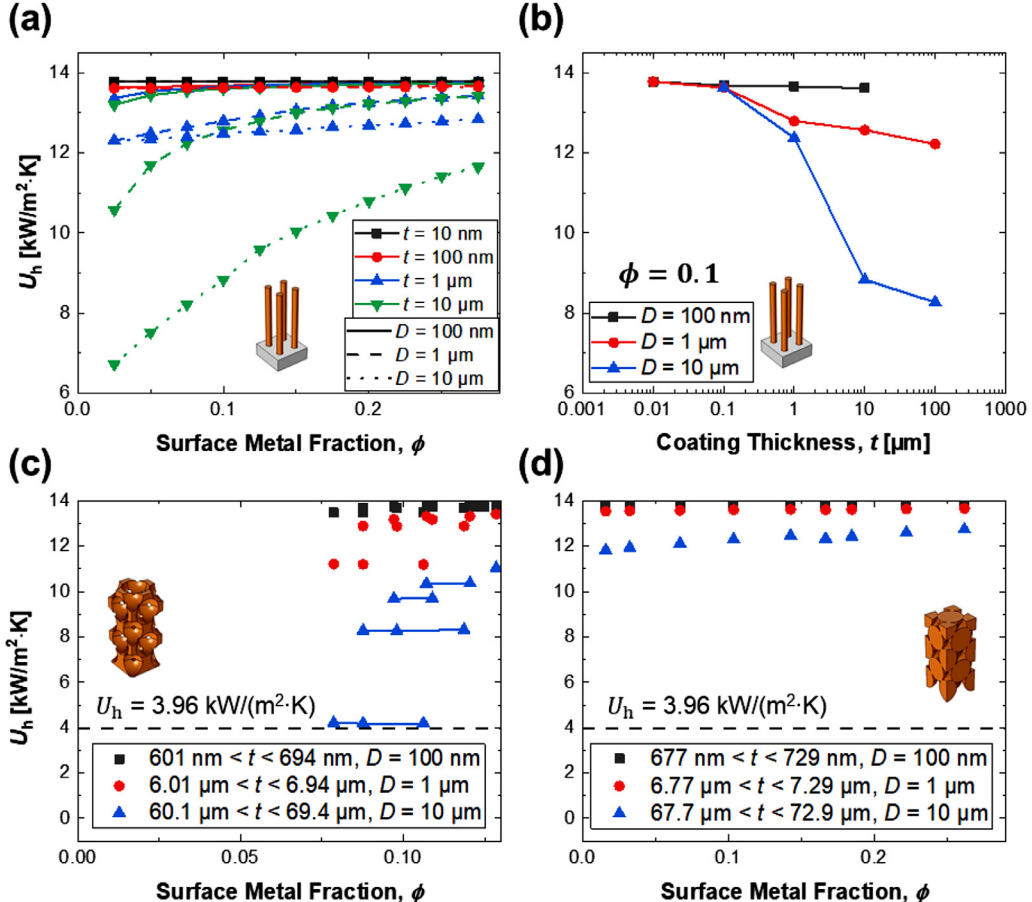


Fig. 10. Simulated overall heat transfer coefficient (U_h) as a function of surface metal fraction and thicknesses of coatings within the regions where dropwise condensation is stable (Fig. 9) for (a) wire, (c) inverse opal, and (d) sintered sphere structures, and (b) wire as a function of coating thickness when the fraction $\phi = 0.1$. Results shown are for varying t or wire diameter (D). (c) The data points with same neck diameters are connected (blue line). (c, d) The black dotted lines (not shown in (a) or (b)) indicate the overall heat transfer coefficient when the filmwise condensation occurs ($U_{h, \text{filmwise}} = 3.96 \text{ kW}/(\text{m}^2 \cdot \text{K})$).

Fig. 10(b) plots U_h as a function of t for a fixed ϕ , and for a variety of wire diameters D . The results show that for nanowires ($D = 100 \text{ nm}$), U_h is higher when compared to the equivalent larger wire diameter coatings. For $t > 10 \mu\text{m}$, a minimum diameter of $D = 1 \mu\text{m}$ is needed to achieve a $< 20\%$ decrease in U_h . Inverse opals can achieve the limit of 20% decrease in overall heat transfer coefficient with $D = 1 \mu\text{m}$ and $6.01 \mu\text{m} < t < 6.94 \mu\text{m}$.

Fig. 11 shows the relationship between overall heat transfer coefficient and the effective thermal conductivity of coatings with different thicknesses and internal heat transfer coefficients. The shaded red region ($k_{\text{eff}} < 0.8 \text{ W}/(\text{m}\cdot\text{K})$) represents state of the art (SOA) hydrophobic coatings. Our work identifies the potential of achieving $k_h \approx 10 \text{ W}/(\text{m}\cdot\text{K})$ while maintaining stable dropwise condensation. Assuming a maximum overall heat transfer coefficient decrease of 71% in order to achieve the filmwise condensation limit with $h_i = 20 \text{ kW}/(\text{m}^2 \cdot \text{K})$ (Fig. 11(a)), our composite coating can be two orders of magnitude thicker when compared to SOA solutions with much greater durability.

For the simulations conducted here, an area-averaged condensation heat transfer coefficient (h_e) was used to represent condensation. However, it is important to point out that small droplets are preferred to achieve higher heat transfer rates, accounting for the majority of heat transfer on the condensing surface during steady condensation. Past works have shown that droplet sizes ranging from $5 \mu\text{m}$ to $100 \mu\text{m}$ in radii account for more than 90% of the overall heat transfer in dropwise condensation [3,55], with larger droplets ($> 100 \mu\text{m}$) mainly responsible for coalescence, collec-

tion, and shedding of liquid, allowing for re-nucleation of small efficient droplets. Therefore, the heat transfer coefficient is non-uniform and highly transient. The non-uniform heat transfer is especially important when the composite coating structure length scale approaches the droplet length scale ($D = 10 \mu\text{m}$) [56,86] as droplets can reside on the metal or polymer and the structure fails to 'look' homogeneous to the droplet residing above. Although the majority of cases simulated here have smaller structure length scale ($D < 10 \mu\text{m}$) when compared to important discrete droplets, additional work is needed to identify the importance of non-homogeneous condensation heat transfer rates on lateral heat spreading. Although simulations conducted using non-uniform heat transfer coefficient with structure length scales and droplet length scales approaching each other ($10 \mu\text{m}$) showed a maximum difference of 15% compared to the uniform condensation heat transfer coefficient results, additional work is needed. Given that the metal structure represents a dominant heat pathway, lateral conduction or the spreading effects are expected to be exacerbated when considering a non-spatially uniform convective boundary conditions, as representative of discrete droplets. This effect is mitigated by the fact that the highly transient nature of dropwise condensation governed by rapid sweeping and re-nucleation makes spatially averaging of heat transfer coefficient appropriate and quite accurate at predicting performance. Future work is needed to study these counterbalancing effects to better quantify their effects on overall conductance from vapor to coolant.

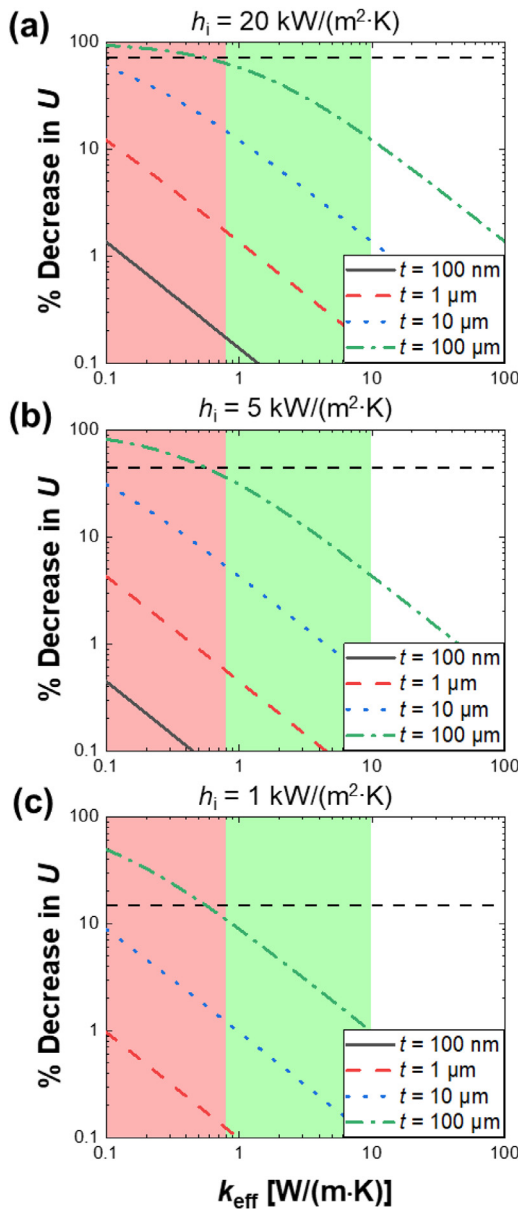


Fig. 11. Percent decrease in overall heat transfer coefficient (U) as a function of composite coating effective thermal conductivity (k_{eff}) for different coating thicknesses (t). Calculated with (a) high ($h_i = 20 \text{ kW}/(\text{m}^2 \cdot \text{K})$), (b) medium ($h_i = 5 \text{ kW}/(\text{m}^2 \cdot \text{K})$), and (c) low ($h_i = 1 \text{ kW}/(\text{m}^2 \cdot \text{K})$) internal convective heat transfer coefficients. As the thickness of the coating increases, U can decrease by an order of magnitude or more depending on k_{eff} . The shaded red region represents SOA hydrophobic coating thermal conductivities, while the shaded green region represents what is possible with the composite structured surfaces presented here. The horizontal black dashed lines indicate the percent decrease with filmwise condensation on external surface.

Although demonstrated here using a rigorous simulation framework, future work is needed to experimentally verify the performance of the proposed structures using thermal conductivity measurement techniques. Typical thermal conductivity measurement techniques such as the 1D calorimetric bar, or 3ω [87,88], or time domain thermo reflectance [89,90], use isothermal boundary conditions, which may not give an accurate prediction for our composite coatings (Fig. 6) operating in a heat exchanger environment. Nevertheless, to get an effective thermal conductivity for isothermal conditions, 3ω would be best suited given the heterogeneous and macroscopic nature of the structures [87,88]. However, an ideal effective thermal conductivity measurement would

require the coating to be tested under convection conditions in a coated pipe exchanging heat between two fluids.

In addition to thermal conductivity characterization, durability characterization using highly accelerated life testing (HALT) is required. The necessity for longevities > 10 years requires the use of HALT approaches at elevated steam temperatures, pressures, and face velocities (erosion) to compare durability with SOA approaches with reasonable test timescales. Furthermore, the inability to create vapor phase, dip, or spray deposition methods of the composite materials motivates the need for further manufacturability and cost analysis. For example, steam condensers used in thermoelectric (natural gas, coal) or nuclear power stations consist of tube bundles exceeding 10,000 tubes. If scalable methods are not developed to apply our composite coatings to existing installations, limited market penetration will occur. If two-step deposition is required (*i.e.* metal structuring followed by polymer infill), metal tube coating prior to assembly and welding may make our approach feasible.

4. Conclusions

In this work, we developed the concept of metal-polymer composite structured coatings to enable durable dropwise condensation heat transfer. To create the high thermal conductivity phase of the composite coating, micro/nanowires, inverse opals, and sintered spheres were studied. Using steady-state 3D FEM heat transfer simulations, we examined the heat transfer performance of the composite coatings as a function of structure size scale, metal volume fraction, overall coating thickness, and surface metal fraction. To predict wettability of our composite coating, we implemented a well-verified model to compute the contact angle hysteresis as a function of surface metal fraction (ϕ), and identified regimes favoring dropwise condensation. Our results demonstrate effective thermal conductivities of $k_h \approx 10, 6$, and $5.2 \text{ W}/(\text{m} \cdot \text{K})$ are achievable with Cu microwire ($\psi = 0.1, \phi = 0.1, t = 10 \mu\text{m}$), Cu inverse opal ($\psi = 0.25, \phi = 0.2, d_n = 14.1 \text{ nm}$), and Cu sintered sphere ($\psi = 0.73, \phi = 0.1, d_n = 14.1 \text{ nm}$) composite structures filled with hydrophobic polymer. Within the identified range of metal surface fraction, the overall heat transfer coefficients using the proposed designs were compared. In the case of thick coatings ($> 10 \mu\text{m}$), wires with diameters $< 1 \mu\text{m}$ or inverse opals with diameters $< 1 \mu\text{m}$ ensured an overall heat transfer coefficient decrease of $< 20\%$ when compared to the ideal and non-durable case of dropwise condensation with no coating. Our work develops a rational design approach to utilize metallic nanostructures for the creation of composite hydrophobic coatings having enhanced durability.

CRediT authorship contribution statement

Ho Chan Chang: Conceptualization, Methodology, Formal analysis, Investigation, Writing - original draft, Visualization. **Manjunath C. Rajagopal:** Methodology, Formal analysis, Investigation, Writing - original draft. **Muhammad Jahidul Hoque:** Conceptualization, Validation, Writing - review & editing. **Junho Oh:** Investigation, Writing - review & editing. **Longnan Li:** Investigation, Writing - review & editing. **Jiaqi Li:** Investigation, Writing - review & editing. **Hanyang Zhao:** Investigation, Writing - review & editing. **Gowtham Kuntumalla:** Investigation, Writing - review & editing. **Sreenath Sundar:** Investigation, Writing - review & editing. **Yuquan Meng:** Investigation, Writing - review & editing. **Chenhui Shao:** Conceptualization, Writing - review & editing, Supervision, Project administration. **Placid M. Ferreira:** Conceptualization, Writing - review & editing, Supervision, Project administration. **Srinivasa M. Salapaka:** Conceptualization, Writing - review & editing, Supervision, Project administration. **Sanjiv Sinha:** Conceptualization, Writing - original draft, Writing

- review & editing, Supervision, Project administration. **Nenad Miljkovic:** Conceptualization, Methodology, Formal analysis, Writing - original draft, Writing - review & editing, Supervision, Project administration.

Acknowledgements

N.M. acknowledges Professor John Rose of Queen Mary University of London for fruitful discussions regarding the concept of composite coatings. This work is supported by the funding from the Office of Naval Research (Grant No. N00014-16-1-2625), and the Advanced Manufacturing Office (AMO) of the Office of Energy Efficiency and Renewable Energy (EERE) under the Department of Energy (DoE) through the contract DE-EE00008312. N.M. and J.O. gratefully acknowledge funding support from the International Institute for Carbon Neutral Energy Research (WPI-I2CNER), sponsored by the Japanese Ministry of Education, Culture, Sports, Science, and Technology.

References

- [1] D. Attinger, C. Frankiewicz, A.R. Betz, T.M. Schutzius, R. Ganguly, A. Das, C.-J. Kim, C.M. Megaridis, Surface engineering for phase change heat transfer: A review, *MRS Energy & Sustainability* 1 (2014).
- [2] H.J. Cho, D.J. Preston, Y. Zhu, E.N. Wang, Nanoengineered materials for liquid-vapour phase-change heat transfer, *Nature Reviews Materials* 2 (2) (2017) 16092.
- [3] R. Enright, N. Miljkovic, J.L. Alvarado, K. Kim, J.W. Rose, Dropwise Condensation on Micro- and Nanostructured Surfaces, *Nanoscale and Microscale Thermophysical Engineering* 18 (3) (2014) 223–250.
- [4] N. Miljkovic, E.N. Wang, Condensation heat transfer on superhydrophobic surfaces, *MRS Bulletin* 38 (5) (2013) 397–406.
- [5] J. Rose, Dropwise condensation theory and experiment: a review, Proceedings of the Institution of Mechanical Engineers, Part A: Journal of Power & Energy 216 (2) (2002) 115–128.
- [6] J. Oh, R.Y. Zhang, P.P. Shetty, J.A. Krogstad, P.V. Braun, N. Miljkovic, Thin Film Condensation on Nanostructured Surfaces, *Advanced Functional Materials* 28 (16) (2018) 1707000.
- [7] T. Foulkes, J. Oh, P. Birbarah, J. Neely, N. Miljkovic, R.C. Pilawa-Podgurski, Active hot spot cooling of GaN transistors with electric field enhanced jumping droplet condensation, in: 2017 IEEE Applied Power Electronics Conference and Exposition (APEC), IEEE, 2017, pp. 912–918.
- [8] N. Miljkovic, D.J. Preston, R. Enright, E.N. Wang, Electrostatic charging of jumping droplets, *Nature Communications* 4 (2013) 2517.
- [9] J. Oh, P. Birbarah, T. Foulkes, S.L. Yin, M. Rentauskas, J. Neely, R.C. Pilawa-Podgurski, N. Miljkovic, Jumping-droplet electronics hot-spot cooling, *Applied Physics Letters* 110 (12) (2017) 123107.
- [10] L.L. Vasiliev, Heat pipes in modern heat exchangers, *Applied thermal engineering* 25 (1) (2005) 1–19.
- [11] H. Andrews, E. Eccles, W. Schofield, J. Badyal, Three-dimensional hierarchical structures for fog harvesting, *Langmuir* 27 (7) (2011) 3798–3802.
- [12] J.C. Love, L.A. Estroff, J.K. Kriebel, R.G. Nuzzo, G.M. Whitesides, Self-assembled monolayers of thiolates on metals as a form of nanotechnology, *Chemical reviews* 105 (4) (2005) 1103–1170.
- [13] A.R. Parker, C.R. Lawrence, Water capture by a desert beetle, *Nature* 414 (6859) (2001) 33.
- [14] H. Zhu, F. Yang, J. Li, Z. Guo, High-efficiency water collection on biomimetic material with superwettable patterns, *Chemical communications* 52 (84) (2016) 12415–12417.
- [15] V.A. Ganesh, H.K. Raut, A.S. Nair, S. Ramakrishna, A review on self-cleaning coatings, *Journal of Materials Chemistry* 21 (41) (2011) 16304–16322.
- [16] K.M. Wisdom, J.A. Watson, X. Qu, F. Liu, G.S. Watson, C.-H. Chen, Self-cleaning of superhydrophobic surfaces by self-propelled jumping condensate, *Proceedings of the National Academy of Sciences* 110 (20) (2013) 7992–7997.
- [17] E. Schmidt, W. Schurig, W. Sellschopp, Versuche über die Kondensation von Wasserdampf in Film- und Tropfenform, *Technische Mechanik und Thermodynamik* 1 (2) (1930) 53–63.
- [18] M. Ahlers, A. Buck-Emden, H.-J. Bart, Is dropwise condensation feasible? A review on surface modifications for continuous dropwise condensation and a profitability analysis, *Journal of Advanced Research* 16 (2019) 1–13.
- [19] J.W. Rose, Theory of Dropwise Condensation, in: *Encyclopedia of Two-Phase Heat Transfer and Flow II*, pp. 1–14.
- [20] K.M. Holden, A.S. Wanniarachchi, P.J. Marto, D.H. Boone, J.W. Rose, The Use of Organic Coatings to Promote Dropwise Condensation of Steam, *Journal of Heat Transfer* 109 (3) (1987) 768–774.
- [21] A.G. Evans, D. Mumm, J. Hutchinson, G. Meier, F. Pettit, Mechanisms controlling the durability of thermal barrier coatings, *Progress in materials science* 46 (5) (2001) 505–553.
- [22] D.L. Burris, W.G. Sawyer, Hierarchically constructed metal foam/polymer composite for high thermal conductivity, *Wear* 264 (3) (2008) 374–380.
- [23] H.S. Kim, H.S. Bae, J. Yu, S.Y. Kim, Thermal conductivity of polymer composites with the geometrical characteristics of graphene nanoplatelets, *Scientific Reports* 6 (2016) 26825.
- [24] C. Huang, X. Qian, R. Yang, Thermal conductivity of polymers and polymer nanocomposites, *Materials Science and Engineering: R: Reports* 132 (2018) 1–22.
- [25] S.M. Hamidinejad, R.K.M. Chu, B. Zhao, C.B. Park, T. Filleter, Enhanced Thermal Conductivity of Graphene Nanoplatelet-Polymer Nanocomposites Fabricated via Supercritical Fluid-Assisted In Situ Exfoliation, *ACS Applied Materials & Interfaces* 10 (1) (2018) 1225–1236.
- [26] T.C. Clancy, S.J.V. Frankland, J.A. Hinkley, T.S. Gates, Multiscale modeling of thermal conductivity of polymer/carbon nanocomposites, *International Journal of Thermal Sciences* 49 (9) (2010) 1555–1560.
- [27] J. Hu, Y. Huang, Y. Yao, G. Pan, J. Sun, X. Zeng, R. Sun, J.-B. Xu, B. Song, C.-P. Wong, Polymer Composite with Improved Thermal Conductivity by Constructing a Hierarchically Ordered Three-Dimensional Interconnected Network of BN, *ACS Applied Materials & Interfaces* 9 (15) (2017) 13544–13553.
- [28] A. Devpura, P. Phelan, R.S. Prasher, Size Effects on the Thermal Conductivity of Polymers Laden with Highly Conductive Filler Particles, *Microscale Thermophysical Engineering* 5 (3) (2001) 177–189.
- [29] Y. Wang, C. Yang, Q.-X. Pei, Y. Zhang, Some Aspects of Thermal Transport across the Interface between Graphene and Epoxy in Nanocomposites, *ACS Applied Materials & Interfaces* 8 (12) (2016) 8272–8279.
- [30] J. Wang, J.K. Carson, M.F. North, D.J. Cleland, A new approach to modelling the effective thermal conductivity of heterogeneous materials, *International journal of heat & mass transfer* 49 (17–18) (2006) 3075–3083.
- [31] J.C. Maxwell, *A treatise on electricity and magnetism*, Clarendon Press, Oxford, 1873.
- [32] D.A.G. Bruggeman, Berechnung verschiedener physikalischer Konstanten von heterogenen Substanzen. I. Dielektrizitätskonstanten und Leitfähigkeiten der Mischkörper aus isotropen Substanzen, 416(7) (1935) 636–664.
- [33] J.D. Albrecht, P.A. Knipp, T.L. Reinecke, Thermal conductivity of opals and related composites, *Physical Review B* 63 (13) (2001) 134303.
- [34] R. Raj, R. Enright, Y. Zhu, S. Adera, E.N. Wang, Unified model for contact angle hysteresis on heterogeneous and superhydrophobic surfaces, *Langmuir* 28 (45) (2012) 15777–15788.
- [35] P.A. Champlin, Techno-economic evaluation of cross-cutting technologies for cost reduction in nuclear power plants, Massachusetts Institute of Technology (2018).
- [36] T.L. Bergman, F.P. Incropera, D.P. DeWitt, A.S. Lavine, *Fundamentals of heat and mass transfer*, John Wiley & Sons, 2011.
- [37] M.C. Rajagopal, H.C. Chang, T. Man, G. Kuntumalla, Y. Meng, S. Sundar, H. Zhao, S. Salapaka, C. Shao, P. Ferreira, N. Miljkovic, S. Sinha, Materials-to-device design of hybrid metal-polymer heat exchanger tubes for low temperature waste heat recovery, *International Journal of Heat and Mass Transfer* 143 (2019) 118497.
- [38] N. Miljkovic, R. Enright, E.N. Wang, Effect of droplet morphology on growth dynamics and heat transfer during condensation on superhydrophobic nanostructured surfaces, *ACS nano* 6 (2) (2012) 1776–1785.
- [39] R. Enright, N. Miljkovic, A. Al-Obeidi, C.V. Thompson, E.N. Wang, Condensation on superhydrophobic surfaces: the role of local energy barriers and structure length scale, *Langmuir* 28 (40) (2012) 14424–14432.
- [40] E. Menke, M. Thompson, C. Xiang, L. Yang, R. Penner, Lithographically patterned nanowire electrodeposition, *Nature materials* 5 (11) (2006) 914.
- [41] K.-H. Chu, R. Xiao, E.N. Wang, Uni-directional liquid spreading on asymmetric nanostructured surfaces, *Nature materials* 9 (5) (2010) 413.
- [42] P.-L. Taberna, S. Mitra, P. Poizot, P. Simon, J.-M. Tarascon, High rate capabilities Fe 3 O 4-based Cu nano-architected electrodes for lithium-ion battery applications, *Nature materials* 5 (7) (2006) 567.
- [43] H. Zhang, X. Yu, P.V. Braun, Three-dimensional bicontinuous ultrafast-charge and-discharge bulk battery electrodes, *Nature nanotechnology* 6 (5) (2011) 277.
- [44] M.T. Barako, A. Sood, C. Zhang, J. Wang, T. Kodama, M. Asheghi, X. Zheng, P.V. Braun, K.E.J.N.I. Goodson, Quasi-ballistic electronic thermal conduction in metal inverse opals, 16(4) (2016) 2754–2761.
- [45] J. Ma, B.R. Parajuli, M.G. Ghosssoub, A. Mihi, J. Sadhu, P.V. Braun, S. Sinha, Coherent phonon-grain boundary scattering in silicon inverse opals, *Nano letters* 13 (2) (2013) 618–624.
- [46] Q.N. Pham, M.T. Barako, J. Tice, Y. Won, Microscale Liquid Transport in Polycrystalline Inverse Opals across Grain Boundaries, *Scientific Reports* 7 (1) (2017) 10465.
- [47] X. Yu, Y.-J. Lee, R. Furstenberg, J.O. White, P.V. Braun, Filling Fraction Dependent Properties of Inverse Opal Metallic Photonic Crystals, 19(13) (2007) 1689–1692.
- [48] M.A. Hanlon, H.B. Ma, Evaporation Heat Transfer in Sintered Porous Media, *Journal of Heat Transfer* 125 (4) (2003) 644–652.
- [49] S.-C. Wong, J.-H. Liou, C.-W. Chang, Evaporation resistance measurement with visualization for sintered copper-powder evaporator in operating flat-plate heat pipes, *International Journal of Heat and Mass Transfer* 53 (19) (2010) 3792–3798.
- [50] Y.Q. Fu, A. Colli, A. Fasoli, J. Luo, A. Flewitt, A. Ferrari, W. Milne, Deep reactive ion etching as a tool for nanostructure fabrication, *Journal of Vacuum Science & Technology B: Microelectronics and Nanometer Structures Processing, Measurement, and Phenomena* 27 (3) (2009) 1520–1526.
- [51] A.T. Paxson, J.L. Yagüe, K.K. Gleason, K.K. Varanasi, Stable Dropwise Condensation for Enhancing Heat Transfer via the Initiated Chemical Vapor Deposition (iCVD) of Grafted Polymer Films, 26(3) (2014) 418–423.

- [52] N. Yoshida, Y. Abe, H. Shigeta, A. Nakajima, H. Ohsaki, K. Hashimoto, T. Watanabe, Sliding Behavior of Water Droplets on Flat Polymer Surface, *Journal of the American Chemical Society* 128 (3) (2006) 743–747.
- [53] R.C. Weast, M.J. Astle, W.H. Beyer, CRC handbook of chemistry and physics, CRC press, Boca Raton, FL, 1988.
- [54] A. Bejan, Convection heat transfer, John wiley & sons, 2013.
- [55] C. Graham, P. Griffith, Drop size distributions and heat transfer in dropwise condensation, *International Journal of Heat and Mass Transfer* 16 (2) (1973) 337–346.
- [56] J.W. Rose, L.R. Glicksman, Dropwise condensation—The distribution of drop sizes, *International Journal of Heat and Mass Transfer* 16 (2) (1973) 411–425.
- [57] J. Rose, The effect of surface thermal conductivity on dropwise condensation heat transfer, *International journal of heat & mass transfer* 21 (1) (1978) 80–81.
- [58] J.W. Rose, Dropwise condensation theory, *International Journal of Heat and Mass Transfer* 24 (2) (1981) 191–194.
- [59] V. Calmudi, R. Mahajan, The effective thermal conductivity of high porosity fibrous metal foams, *Journal of Heat Transfer* 121 (2) (1999).
- [60] C. Tjoen, Y. Park, Q. Wang, A. Sommers, X. Han, A. Jacobi, A review on polymer heat exchangers for HVAC&R applications, *International journal of refrigeration* 32 (5) (2009) 763–779.
- [61] P.E. Hopkins, Thermal transport across solid interfaces with nanoscale imperfections: effects of roughness, disorder, dislocations, and bonding on thermal boundary conductance, *ISRN Mechanical Engineering* 2013 (2013).
- [62] T. Luo, G. Chen, Nanoscale heat transfer—from computation to experiment, *Physical Chemistry Chemical Physics* 15 (10) (2013) 3389–3412.
- [63] C. Zhang, S. Lingamneni, M.T. Barako, J.W. Palko, M. Asheghi, K.E. Goodson, Characterization of the capillary performance of copper inverse opals, in: 2016 15th IEEE Intersociety Conference on Thermal and Thermomechanical Phenomena in Electronic Systems (ITHERM), 2016, pp. 1035–1039.
- [64] Y.P. Mamunya, V.V. Davydenko, P. Pissis, E.V. Lebedev, Electrical and thermal conductivity of polymers filled with metal powders, *European Polymer Journal* 38 (9) (2002) 1887–1897.
- [65] D. Kumlutas, I.H. Tavman, A Numerical and Experimental Study on Thermal Conductivity of Particle Filled Polymer Composites, 19(4) (2006) 441–455.
- [66] B.-X. Wang, L.-P. Zhou, X.-F. Peng, A fractal model for predicting the effective thermal conductivity of liquid with suspension of nanoparticles, *International Journal of Heat & Mass Transfer* 46 (14) (2003) 2665–2672.
- [67] S. Kirkpatrick, Percolation and Conduction, *Reviews of Modern Physics* 45 (4) (1973) 574–588.
- [68] G. Zhang, Y. Xia, H. Wang, Y. Tao, G. Tao, S. Tu, H. Wu, A Percolation Model of Thermal Conductivity for Filled Polymer Composites, 44(8) (2010) 963–970.
- [69] K. Pietrak, T.S. Wiśniewski, A review of models for effective thermal conductivity of composite materials, *Journal of Power Technologies* 95 (1) (2014) 14–24.
- [70] H.S. Tekce, D. Kumlutas, I.H. Tavman, Effect of Particle Shape on Thermal Conductivity of Copper Reinforced Polymer Composites, 26(1) (2007) 113–121.
- [71] D.J. Preston, N. Miljkovic, J. Sack, R. Enright, J. Queeney, E.N. Wang, Effect of hydrocarbon adsorption on the wettability of rare earth oxide ceramics, 105(1) (2014) 011601.
- [72] X. Yan, Z. Huang, S. Sett, J. Oh, H. Cha, L. Li, L. Feng, Y. Wu, C. Zhao, D. Orejon, F. Chen, N. Miljkovic, Atmosphere-Mediated Superhydrophobicity of Rationally Designed Micro/Nanostructured Surfaces, *ACS Nano* 13 (4) (2019) 4160–4173.
- [73] S. Takeda, M. Fukawa, Y. Hayashi, K. Matsumoto, Surface OH group governing adsorption properties of metal oxide films, *Thin Solid Films* 339 (1) (1999) 220–224.
- [74] F.-M. Chang, S.-L. Cheng, S.-J. Hong, Y.-J. Sheng, H.-K. Tsao, Superhydrophilicity to superhydrophobicity transition of CuO nanowire films, 96(11) (2010) 114101.
- [75] T.-S. Wong, S.H. Kang, S.K.Y. Tang, E.J. Smythe, B.D. Hatton, A. Grinthal, J. Aizenberg, Bioinspired self-repairing slippery surfaces with pressure-stable omniphobicity, *Nature* 477 (7365) (2011) 443–447.
- [76] S. Sett, X. Yan, G. Barac, L.W. Bolton, N. Miljkovic, Lubricant-Infused Surfaces for Low-Surface-Tension Fluids: Promise versus Reality, *ACS Applied Materials & Interfaces* 9 (41) (2017) 36400–36408.
- [77] S. Anand, A.T. Paxson, R. Dhiman, J.D. Smith, K.K. Varanasi, Enhanced Condensation on Lubricant-Impregnated Nanotextured Surfaces, *ACS Nano* 6 (11) (2012) 10122–10129.
- [78] J.D. Smith, R. Dhiman, S. Anand, E. Reza-Garduno, R.E. Cohen, G.H. McKinley, K.K. Varanasi, Droplet mobility on lubricant-impregnated surfaces, *Soft Matter* 9 (6) (2013) 1772–1780.
- [79] B.R. Solomon, S.B. Subramanyam, T.A. Farnham, K.S. Khalil, S. Anand, K.K. Varanasi, CHAPTER 10 Lubricant-Impregnated Surfaces, Non-wettable Surfaces: Theory, Preparation and Applications, The Royal Society of Chemistry (2017) 285–318.
- [80] L. Wang, T.J. McCarthy, Covalently Attached Liquids: Instant Omnipobic Surfaces with Unprecedented Repellency, 55(1) (2016) 244–248.
- [81] H. Cha, H. Vahabi, A. Wu, S. Chavan, A.K. Kota, N. Miljkovic, The Role of Surface Wettability on Dropwise Condensation, in: Proceedings of the 6th Micro and Nano Flows Conference, MNF2018, Atlanta, GA, 2018.
- [82] A. Wu, H. Vahabi, H. Cha, S. Chavan, A. Kota, N. Miljkovic, Dropwise Condensation on Hydrophilic Surfaces, in: Proceedings of The 10th International Conference on Boiling & Condensation Heat Transfer, ICBCHT2018, Nagasaki, Japan, 2018.
- [83] H. Cha, H. Vahabi, A. Wu, S. Chavan, M.-K. Kim, S. Sett, S.A. Bosch, W. Wang, A.K. Kota, N. Miljkovic, Dropwise Condensation on Solid Hydrophilic Surfaces, *Science Advances*, (in press).
- [84] J. Ma, H. Cha, M.-K. Kim, D.G. Cahill, N. Miljkovic, Condensation Induced Delamination of Nanoscale Hydrophobic Films, *Advanced Functional Materials*, (2019) 1905222.
- [85] P.J. Marto, D.J. Looney, J.W. Rose, A.S. Wanniarachchi, Evaluation of organic coatings for the promotion of dropwise condensation of steam, *International Journal of Heat and Mass Transfer* 29 (8) (1986) 1109–1117.
- [86] E. Le Fevre, J.W. Rose, A theory of heat transfer by dropwise condensation, in: *International Heat Transfer Conference Digital Library*, Begel House Inc (1966).
- [87] D.G. Cahill, Thermal conductivity measurement from 30 to 750 K: the 3ω method, 61(2) (1990) 802–808.
- [88] C. Dames, Measuring the thermal conductivity of thin films: 3 omega and related electrothermal methods, *Annual Review of Heat Transfer* 16 (2013).
- [89] D.G. Cahill, Thermal-conductivity measurement by time-domain thermoreflectance, *MRS Bulletin* 43 (10) (2018) 782–789.
- [90] P. Jiang, X. Qian, R. Yang, Time-domain thermoreflectance (TDTR) measurements of anisotropic thermal conductivity using a variable spot size approach, 88(7) (2017) 074901.